ARTICLE IN PRESS

Earth-Science Reviews xxx (xxxx) xxx-xxx

FISFVIFR

Contents lists available at ScienceDirect

Earth-Science Reviews

journal homepage: www.elsevier.com/locate/earscirev



Sulfur-isotope evidence for recovery of seawater sulfate concentrations from a PTB minimum by the Smithian-Spathian transition

Alan Stebbins^{a,*}, Thomas J. Algeo^{b,c}, Christian Olsen^d, Hiroyoshi Sano^e, Harold Rowe^f, Robyn Hannigan^a

- School for the Environment, University of Massachusetts Boston, Boston, MA 02125, USA
- ^b Department of Geology, University of Cincinnati, Cincinnati, OH 45221, USA
- ^c State Key Laboratories of BGEG and GPMR, China University of Geosciences, Wuhan 430074, China
- ^d College of Engineering and Physical Sciences, University of New Hampshire, Durham, NH 03823, USA
- ^e Department of Earth and Planetary Sciences, Kyushu University, Fukuoka 812-8581, Japan
- f Bureau of Economic Geology, The University of Texas at Austin, Austin, TX, USA

ARTICLE INFO

Keywords: SSB Jesmond Cache Creek Terrane Western Canada Carbonate-associated sulfate Pyrite

ABSTRACT

The Smithian-Spathian substage boundary (SSB) in the Early Triassic was an important time interval during the protracted recovery of marine faunas and ecosystems following the end-Permian mass extinction event. Although some Tethyan SSB sections have been studied, little information is available regarding environmental conditions in the Panthalassic Ocean, which comprised ~85% of the Early Triassic global ocean, during the Smithian-Spathian transition. Understanding changes in the carbon and sulfur cycles during the Early Triassic is important for deciphering the pattern and controls on the marine recovery. Our understanding of the Early Triassic sulfur cycle, in particular, is incomplete. In this study, we report carbonate carbon and oxygen, carbonate-associated sulfate (CAS) sulfur and oxygen, and pyritic sulfur isotopic ratios from the Jesmond section, Cache Creek Terrane, western Canada. This section, which formed as a tropical carbonate atoll in the middle of the Panthalassic Ocean, spans the latest Smithian to middle Spathian. Both $\delta^{34}S_{CAS}$ and $\delta^{18}O_{CAS}$ increased through the SSB transition before decreasing in the early Spathian, matching variation in the $\delta^{13}C_{carb}$ profile. We hypothesize that the sharp increase in $\delta^{34}S_{CAS}$ and $\delta^{18}O_{CAS}$ at the SSB reflects a global increase in the amount of microbial sulfate reduction (MSR) and pyrite burial. Driving this increase in MSR and pyrite burial were cooling temperatures, increasing primary productivity, and increasing organic matter availability. The decreasing trend immediately following the SSB indicates that these environmental changes reached maxima and began to diminish or reverse in the early Spathian. The difference between $\delta^{34}S_{CAS}$ and $\delta^{34}S_{pyr}$ values ($\Delta^{34}S_{CAS-pyr}$) remained relatively stable from the latest Smithian through the middle Spathian. This stability provides an estimate of MSR sulfur-isotope depletion allowing us to estimate paleo-seawater sulfate concentrations. Using the "MSRtrend" method, we estimate that Early Triassic seawater sulfate concentrations were between 2.5 and 9.1 mM. These estimates are higher than previously published values for the Permian-Triassic boundary, suggesting an overall increase in seawater sulfate by the late Early Triassic.

1. Introduction

The Smithian-Spathian substage boundary (SSB) of the Early Triassic was a major turning point in the recovery from the Permian-Triassic boundary (PTB) crisis. Zircon U—Pb dating places the SSB about 1.3 Myr (250.6 Ma; Ovtcharova et al., 2006) after the PTB (251.9 Ma; Burgess et al., 2014). The SSB witnessed major changes in marine environmental and global climatic conditions as well as a partial recovery of marine ecosystems (Fig. 1). The late Smithian was a time of

hyperwarming, as documented by conodont oxygen isotopes (Sun et al., 2012; Romano et al., 2013), triggering a crisis among ammonoids (Brayard et al., 2006; Brühwiler et al., 2010; Stanley, 2009), conodonts (Orchard, 2007; Stanley, 2009), some benthic communities (Hofmann et al., 2014; Foster et al., 2017), and a size reduction (Lilliput effect) occurred among surviving conodont taxa (Chen et al., 2013). Terrestrial ecosystems also experienced turnover at that time (Galfetti et al., 2007; Hermann et al., 2012; Hochuli et al., 2016). Recovery from the late Smithian crisis began in the earliest Spathian, as exemplified by the

E-mail address: alan.stebbins001@umb.edu (A. Stebbins).

https://doi.org/10.1016/j.earscirev.2018.08.010

Received 28 December 2017; Received in revised form 11 June 2018; Accepted 22 August 2018 0012-8252/ © 2018 Elsevier B.V. All rights reserved.

^{*} Corresponding author.

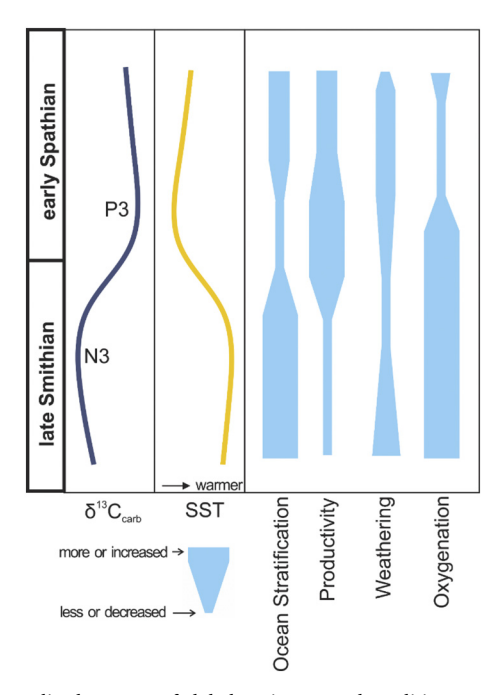


Fig. 1. Generalized patterns of global environmental conditions across the SSB. A relatively wider bar suggests an increase in that environmental condition and vice versa. For example, ocean stratification was strongest during the late Smithian, weakened through the SSB, and increased again in the early Spathian. Data: $\delta^{13}C_{carb}$ (Song et al., 2013); sea-surface temperatures (SST; Sun et al., 2012; Romano et al., 2013); stratification and productivity (Song et al., 2013); weathering (Song et al., 2015); redox conditions (Song et al., 2012; Grasby et al., 2013a; Tian et al., 2014; Wei et al., 2015; Wignall et al., 2015; Clarkson et al., 2016; Huang et al., 2017).

newly discovered and diverse Paris Biota from the western U.S. (Brayard et al., 2017). At that time, global cooling (Sun et al., 2012; Romano et al., 2013) led to a steepening of the latitudinal temperature gradient and a contraction of the paleolatitudinal range of surviving ammonoid taxa (Brayard et al., 2006). Speculatively, these changes marked a major reduction in levels of magmatic activity within the Siberian Traps Large Igneous Province (Grasby et al., 2015; Shen et al., in review).

Carbon cycle changes at the SSB are well documented: marine carbonate carbon-isotope records show a rapid (\sim 100 kyr), large (\sim 5‰) positive excursion across this boundary (Payne et al., 2004; Corsetti et al., 2005), from the late Smithian N3 minimum to the early Spathian P3 maximum (per the terminology of Song et al., 2013; Fig. 1). In contrast, the Early Triassic sulfur cycle has received much less attention to date. To help further decipher marine environmental conditions during the Early Triassic recovery, we combined detailed knowledge of the carbon cycle with a growing understanding of the sulfur cycle.

The sulfur cycle of the Permian-Triassic has been investigated for certain time windows, such as the Late Permian through Dienerian and parts of the Middle Triassic (Luo et al., 2010; Song et al., 2014; Schobben et al., 2015; Bernasconi et al., 2017, and references therein). On the other hand, the sulfur cycle during the Smithian-Spathian transition has received little attention to date. Evaporite δ^{34} S data, compiled at the substage level for the Smithian and Spathian, exhibit a wide range of values (Holser, 1984; Marenco, 2007; Marenco et al., 2008; Horacek et al., 2010; Bernasconi et al., 2017), which may reflect large changes in sulfur cycling at that time. High-resolution evaporite δ^{34} S profiles for these substages are rare, however (Horacek et al., 2010; Bernasconi et al., 2017), and the few temporally resolved CAS studies from the eastern Paleo-Tethys (South China) and southern Neo-Tethys (Spiti Valley, India) do not clearly define global substage trends

(Song et al., 2014; Zhang et al., 2015; Stebbins, 2018; Stebbins et al., 2018).

Relatively little is known about the massive Panthalassic Ocean, which comprised > 85% of the global ocean during the Early Triassic. Most information originates from four areas: (1) the western Pangean continental margin in western U.S. and Canada (Schoepfer et al., 2012; Schoepfer et al., 2013; Hofmann et al., 2014; Olivier et al., 2016; Brayard et al., 2017; Zhang et al., 2017, and references therein); (2) the mid-Panthalassic deep ocean in Japan (Isozaki, 1997; Algeo et al., 2010; Wignall et al., 2010; Algeo et al., 2011; Takahashi et al., 2015; Zhang et al., 2017, and references therein); (3) shallow atoll carbonates in Japan (Sano and Nakashima, 1997; Horacek et al., 2009; Isozaki, 2009; Zhang et al., in press, and references therein); and (4) the southwestern continental slope in New Zealand (Aita and Spörli, 2007; Takemura et al., 2007; Yamakita et al., 2007; Hori et al., 2011; Takahashi et al., 2013). The Jesmond section represents a shallowwater carbonate succession in the Cache Creek Terrane of western Canada (Sano et al., 2012). For this study, we analyzed the sulfur-isotope ratios of carbonate rocks from the Jesmond section to reconstruct paleoenvironmental conditions recorded in the central Panthalassic Ocean during the SSB transition. Our main goal is not to reconstruct local events at Jesmond but to identify and interpret the global longterm variation of seawater sulfate isotope values across the SSB.

2. Marine carbon-sulfur cycles

Microbial sulfate reduction (MSR) links the marine sulfur and carbon cycles. Tracking temporal changes in both cycles can provide important information for paleoenvironmental reconstruction. One of the more insightful tools for tracking changes to the sulfur cycle is the sulfur-isotope composition of seawater sulfate and pyrite (Claypool et al., 1980; Strauss, 1997). MSR occurs in a series of steps where the lighter ³²S isotope is more favorably incorporated into reduced sulfur species relative to the heavier ³⁴S isotope (e.g., Rees, 1973; Brunner and Bernasconi, 2005). The final hydrogen sulfide product of MSR can have δ^{34} S values > 60% less than the residual sulfate (Sim et al., 2011). The actual fractionation is mainly based on the rate of MSR (Leavitt et al., 2013) or sulfate concentrations (Algeo et al., 2015). Depending on environmental conditions much of the hydrogen sulfide produced by MSR will oxidize back into the sulfate pool (Jorgensen, 1982). This returns its lighter isotopic composition to the seawater sulfate pool. Hydrogen sulfide that is not re-oxidized can remain in the watercolumn creating inhospitable euxinic conditions (e.g., Kump et al., 2005; Schobben et al., 2016a) or be removed from the system through the formation and burial of pyrite. Therefore, increases in the amount of MSR and pyrite burial increase seawater sulfate δ^{34} S. Other major factors that influence the $\delta^{34}S$ value of seawater sulfate include weathering and volcanism fluxes (Fig. 2). Both of these inputs are typically ³²S-enriched compared to the marine sulfate pool so increased fluxes will lower seawater sulfate δ^{34} S values (Bottrell and Newton, 2006). Additionally, during most steps of MSR, the oxygen isotopes of seawater sulfate fractionate similarly to sulfur isotopes (Mizutani and Rafter, 1969; Brunner et al., 2005). However, unlike sulfur, the oxygen isotopes of various intermediate species can exchange oxygen atoms with ambient water through an equilibrium isotope effect (Mizutani and Rafter, 1973; Fritz et al., 1989). This difference can provide further paleoenvironmental constraint (e.g., Schobben et al., 2015).

In the geologic record, we can use the isotope values of carbonate-associated-sulfate (CAS) and pyrite as a proxy for the seawater sulfate $\delta^{34}S$ and $\delta^{18}O$ and hydrogen sulfide $\delta^{34}S$. CAS is a trace amount of sulfate that structurally substitutes into the carbonate lattice (Takano, 1985). CAS faithfully records the sulfate $\delta^{34}S$ and $\delta^{18}O$ composition of the fluids from which the carbonate precipitated (Kampschulte and Strauss, 1998; Kampschulte and Strauss, 2004; Bottrell and Newton, 2006, and references therein). Whole-rock $\delta^{34}S_{CAS}$, $\delta^{18}O_{CAS}$, and $\delta^{34}S_{pyr}$ represent an average isotope composition of all CAS or pyrite within the

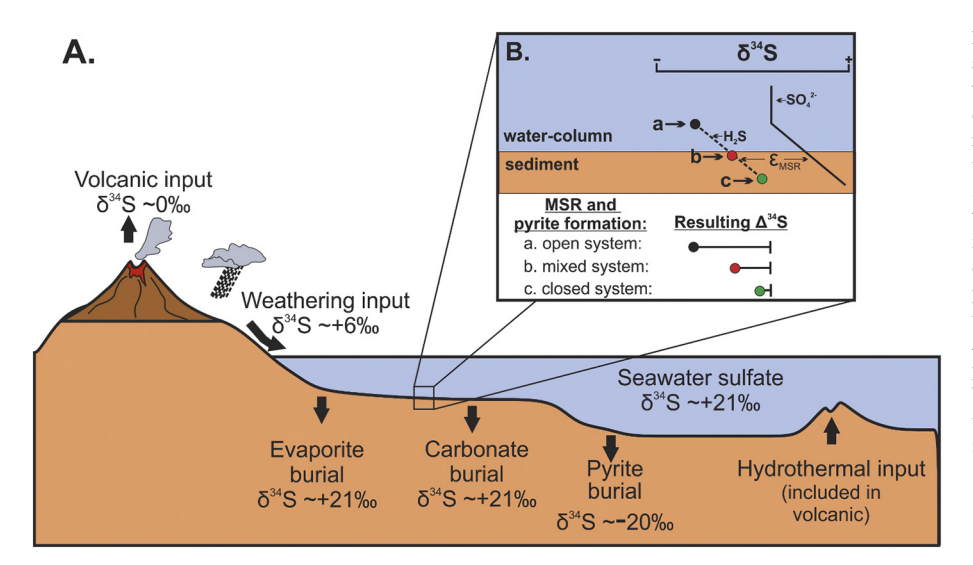


Fig. 2. (A) Simplified geologic sulfur cycle showing seawater sulfate inputs (volcanic, hydrothermal, and weathering) and outputs (pyrite, carbonate, and evaporite burial). The δ^{34} S values are estimates of modern values to exemplify the differences between the inputs and outputs (modified from Fike et al., 2015). (B) A simplified sediment-water interface with various locations of pyrite formation (modified from Gomes and Hurtgen, 2015). The different locations of pyrite formation result in different proportions of open- vs. closed-system pyrite that determine the whole-rock $\delta^{34}S_{pyr}$ value. The resulting Δ^{34} S will vary based on the open or closed nature of pyrite formation. The apparent depletion recorded by $\Delta^{34}S_{CAS-DVI}$ in the geologic record will be smaller than the depositional MSR fractionation (ϵ_{MSR}) if it incorporated any closed-system pyrite.

sample. For CAS isotopes, different carbonate components can vary in their S- and O-isotopic compositions due to early or burial diagenesis such that the whole-rock average may not correspond exactly to contemporaneous seawater sulfate values (Present et al., 2015; Fichtner et al., 2017). For example, Bernasconi et al. (2017) found that $\delta^{34}S_{CAS}$ values around the PTB were 34S-enriched compared to age-equivalent $\delta^{34}S_{evaporite}$ values, but both proxies recorded a similar first-order trend in the earliest Triassic. A careful evaluation of potential alteration to whole-rock δ³⁴S_{CAS} values is necessary prior to interpretation of depositional trends. Similarly, whole-rock $\delta^{34}S_{pvr}$ values include pyrite formed during different stages of diagenesis (i.e., open versus closed porewater systems; Gomes and Hurtgen, 2015). "Open system" and "closed system" refer to the endmember scenarios defined by sulfate diffusion and availability in the MSR zone. Limited diffusion and availability of seawater sulfate occurs under closed-system conditions, resulting in increased δ³⁴S of H₂S and pyrite due to Rayleigh isotope distillation (Fig. 2; e.g., Chambers and Trudinger, 1979). Rayleigh isotope distillation does not affect $\delta^{34}S$ in open systems due to the unlimited availability of sulfate. If a sample incorporates any amount of closed-system pyrite, the resulting whole-rock $\delta^{34}S_{pyr}$ will be relatively higher than the open-system ratio. Under closed-system conditions, residual sulfate that is strongly enriched in ³⁴S due to Rayleigh isotope distillation can also be incorporated into the whole-rock $\delta^{34}S_{\text{CAS}}$ value. However, whole-rock $\delta^{34}S_{CAS}$ can potentially be buffered against this contribution and retain original seawater sulfate isotope values (Lyons et al., 2004; Rennie and Turchyn, 2014), although this is not always the case (Present et al., 2015). This is important for interpretations of paleoenvironmental data. For example, when using the difference between $\delta^{34}S_{CAS}$ and $\delta^{34}S_{pyr}$ ($\Delta^{34}S_{CAS-pyr}$) as a proxy for the isotopic depletion due to MSR (e.g., Algeo et al., 2015). If $\delta^{34}S_{pyr}$ reflects primarily open-system conditions, then $\Delta^{34}S_{CAS-pyr}$ records MSR depletion (Fig. 2). However, since CAS and pyrite form in different parts of the water-column or porewaters, it is also possible that $\Delta^{34}S_{CAS-pvr}$ records an "apparent depletion" value (Fig. 2; Lyons et al., 2004; Riccardi, 2007; Rennie and Turchyn, 2014; Gomes and Hurtgen, 2015). Apparent depletion values are influenced by open- versus closed-system conditions, which depend on the depth below the sediment-water interface at which MSR occurs, the connectedness of the sediment pore system with the overlying water-column, and porewater redox conditions (Gomes et al., 2016).

3. Geologic background

3.1. The Jesmond section

The study area is in the Cache Creek Terrane, which is an accretionary terrane of the Canadian Cordillera (Monger et al., 1991). The terrane became part of the western margin of North America during the Jurassic and contains stratigraphically discontinuous Mississippian to Jurassic aged deposits (Monger et al., 1991; Orchard et al., 2001; Struik et al., 2001; Sano et al., 2012). Although the exact location of the Cache Creek Terrane within the Early Triassic Panthalassic Ocean is uncertain (e.g., Johnston and Borel, 2007), it was probably between 0 and 30°N and closer to the western boundary of Pangea than to the eastern boundary (Fig. 3B). The Marble Range area of southern British Columbia, western Canada contains many Triassic carbonate sections (Beyers and Orchard, 1989, 1991) including Jesmond (Fig. 3A; Sano et al., 2012).

The Jesmond section is a 91-m-thick composite of carbonatedominated outcrops exposed in the northern end of the Marble Range (Figs. 3A, 4; Sano et al., 2012). The section was divided into three lithologic units by Sano et al. (2012) based on a detailed facies analysis (Fig. 4). The lower unit, from the base of the outcrop to about 17 m, consists mostly of peloidal grainstone, packstone, and mudstonewackestone. All three facies represent deposition on an intertidal mudflat (Sano et al., 2012). Thin calcareous shale at 12.5 to 14 m may represent a short interval of subaerial exposure (Fig. 4). Thick beds of dolomicrite dominate the middle unit, from about 17 to 61.5 m, with minor beds of flat-pebble conglomerates, stromatolitic bindstones, peloidal bindstones, skeletal limestone, and oolitic grainstone (Fig. 4). The dolomicrite is fine-grained and formed by syngenetic growth with no signs of supratidal deposition (Sano et al., 2012). The dolomicrite represents an intertidal mudflat environment, and the flat-pebble conglomerates are indicative of intermittent storm deposits (Sano et al., 2012). The other facies of the middle unit suggest shallow subtidal mudflats or sand bars. The upper unit, from 61.5 m to the top of the section at 91 m, contains thick beds of peloidal mudstone and packstone with minor intercalations of skeletal limestones and flat-pebble conglomerates. Microgastropods occur throughout the entire section and smaller foraminifers are scattered in the middle and upper units. The carbonate microfacies of the study section are consistent with (1) deposition on a tropical atoll, mainly within a low-energy central lagoon that was intermittently disturbed by storms; (2) repeated shallowing of the lagoon, producing a sequence of 12 shallow subtidal to (occasionally) intertidal cycles; (3) an overall increase in water depths from the lower to the upper unit; (4) great distance from any landmasses, as

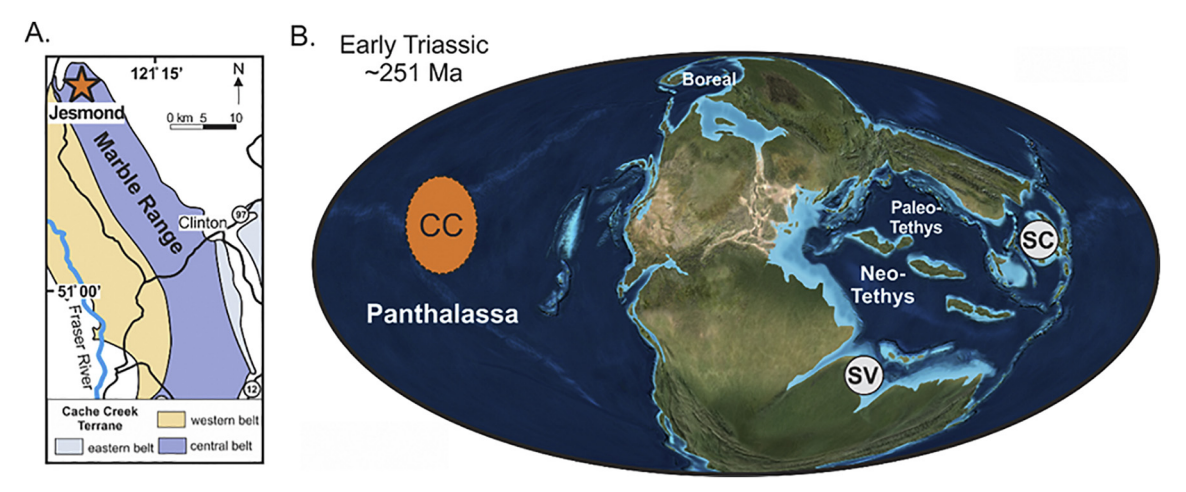


Fig. 3. (A) Geologic map of the Cache Creek Terrane in southern British Columbia, Canada (after Sano et al., 2012). The star marks the location of the Jesmond section within the Marble Range. (B) Paleogeographic map of the Early Triassic world (modified from Colorado Plateau Geosystems image, updated by Ron Blakey, 2018). The locations of the Cache Creek Terrane (CC) in the Panthalassic Ocean is approximate; also shown are the Spiti Valley (SV) and South China (SC).

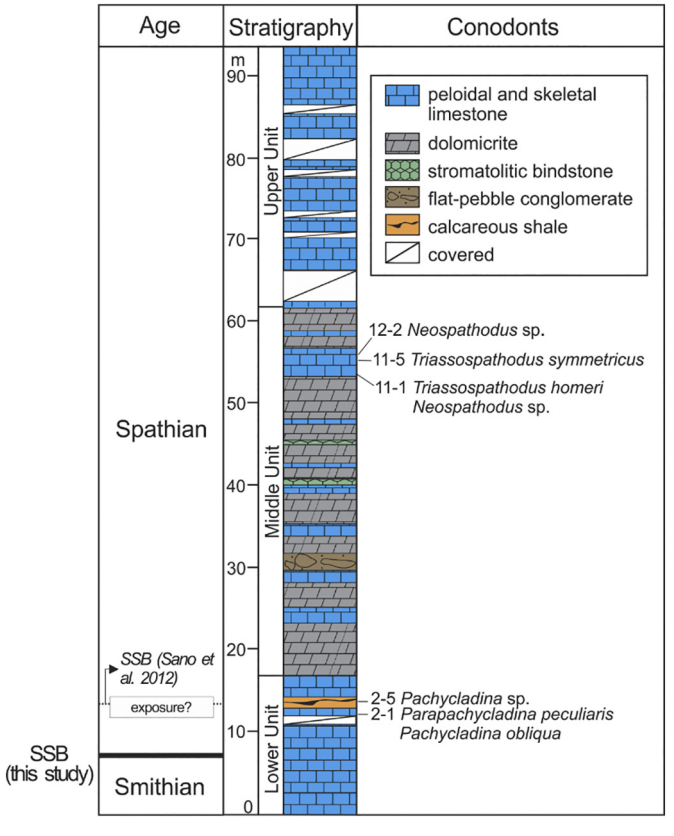


Fig. 4. The age designation, generalized lithology, and conodont fossils for the Jesmond section (after Sano et al., 2012). Their preliminary placement of the Smithian-Spathian boundary (SSB) at \sim 14 m was based on conodont biostratigraphic data, but the present study suggests a lower placement of the SSB (at 7.1 m) based on a high-resolution $\delta^{13}C_{carb}$ profile.

shown by a near-lack of terrigenous material; and (5) no indication of oxygen limitation (Sano et al., 2012).

3.2. Placement of the SSB at Jesmond

The Jesmond section has moderately good biostratigraphic control. The conodonts *Pachycladina obliqua*, *Parapachycladina peculiaris*, and *Pachycladina* sp. were found sparsely distributed within the lower unit (Fig. 4; Sano et al., 2012). These fossils are of late Smithian age, and the

SSB was placed directly above this level, close to or within a subaerial exposure horizon between about 12 and 14 m (Sano et al., 2012). For the middle to upper units, *Triassospathodus homeri*, *T. symmetricus*, and *Neospathodus* sp. are distinctive members of the early Spathian *T. homeri* group (Sano et al., 2012). The earliest Spathian *Novispathodus ping-dingshanensis* and the *Icriospathodus collinsoni* zones, which predate the *T. homeri* Zone in some SSB sections (Kozur, 2003; Chen et al., 2015), were not identified at Jesmond. The top of the Jesmond section is regarded as mid-Spathian in age (Sano et al., 2012).

Carbon-isotope stratigraphy supports these age assignments, while allowing a refined placement of the SSB (Fig. 4). Globally, the SSB corresponds closely to the midpoint of the positive carbon-isotope excursion (CIE) from the late Smithian minimum (N3) to the earliest Spathian maximum (P3) (Zhang et al., in review; note: numbering of Early Triassic CIEs per Song et al., 2013, 2014). At Jesmond, the positive N3-to-P3 CIE that straddles the SSB is present between 3 and 8 m, with a midpoint value at 7.1 m (Fig. 5). Although it is unclear whether the $\delta^{13}C_{carb}$ values of $\sim 0\%$ at the base of the Jesmond section record the absolute N3 minimum, they are likely to be close to it because another shallow-water mid-Panthalassic section (Kamura, Japan) yields a well-defined N3 minimum of ~0% (Horacek et al., 2009; Zhang et al., in press). Carbon-isotope stratigraphy limits the placement of the SSB at Jesmond to no higher than 8 m, i.e., the level of the P3 $\delta^{13}C_{carb}$ maximum, which is slightly younger than the SSB. The midpoint of the N3-to-P3 CIE is at 7.1 m, which is our estimate of the location of the SSB, and which is \sim 5 to 7 m lower than the SSB of Sano et al. (2012).

The age of the top of the Jesmond section can be approximately constrained based on C-isotope chemostratigraphy. A negative global CIE (P3-to-N4) that occurred during the early to mid-Spathian *T. homeri* Zone (Song et al., 2013, and references therein) makes up most of the Jesmond $8^{13}C_{\rm carb}$ profile, beginning at the P3 level (8 m) and extending to the top of the section. $8^{13}C_{\rm carb}$ values appear to reach a minimum (0–1‰) at 88 m, although the trend in the upper part of the section (at 88–92 m) is not well-defined, so it is uncertain whether the 88-m level actually corresponds to the N4 CIE minimum. However, $8^{13}C_{\rm carb}$ values of 0–1‰ are typical of the N4 minimum (e.g., Tong et al., 2007; Song et al., 2013), so the top of the Jesmond section is likely to be quite close to the N4 CIE if it is not at 88 m. Thus, C-isotope stratigraphy is consistent with conodont biostratigraphic data suggesting a mid-Spathian age for the top of the Jesmond section.

4. Methods

Unless otherwise noted, all extractions and analyses were performed

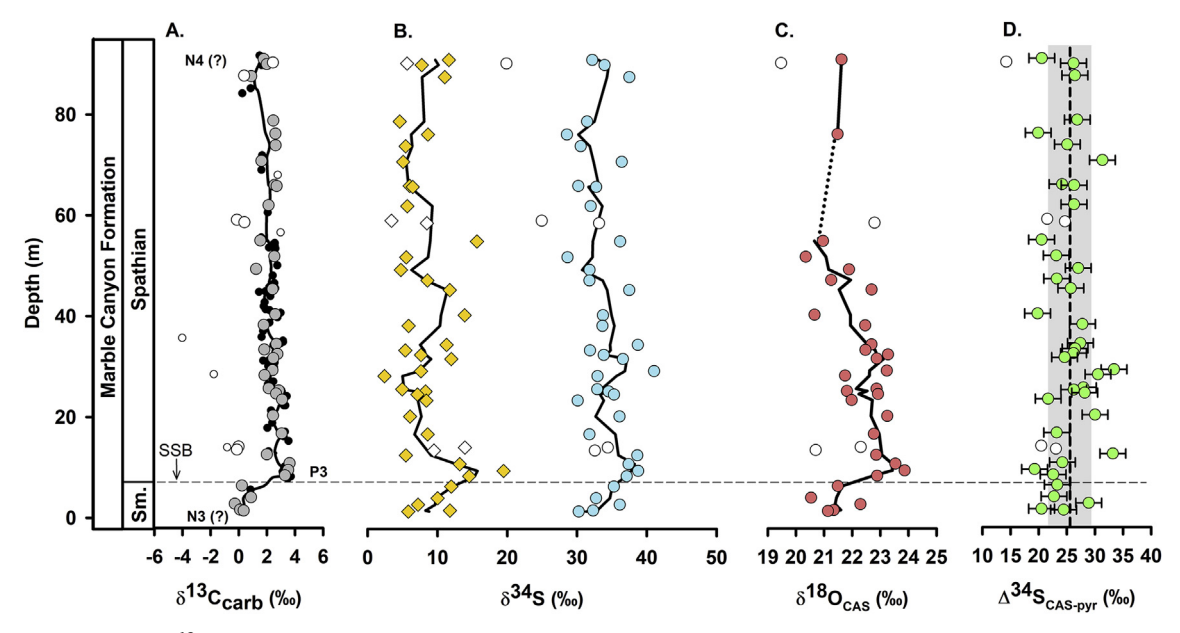


Fig. 5. Stratigraphic trends (A) $\delta^{13}C_{carb}$, the larger markers (gray) represent samples extracted for CAS and pyrite. The smaller markers (black) represent carbonate samples not extracted for CAS or pyrite. The white markers represent screened samples (Section 6.1.1). We updated the SSB location based on the $\delta^{13}C_{carb}$ values (Zhang et al., in review). The N3, P3, and N4 nomenclature follows Song et al. (2013); "?" indicates uncertainty whether the C-isotope minima at the base and top of the section are the true N3 and N4 minima. (B) δ^{34} S values of CAS (circles) and pyrite (diamonds). (C) $\delta^{18}O_{CAS}$ values. Dotted line is an unmeasured interval. (D) $\Delta^{34}S_{CAS-pyr}$ values. The dashed line and box represent the average \pm standard deviation of the entire $\Delta^{34}S_{CAS-pyr}$ dataset. The black line in A is a five-point moving average, and in B-D a three-point moving average to identify the long-term patterns. Our estimated error for $\delta^{34}S_{CAS}$ (S.D. = 1.23‰) and $\delta^{34}S_{pyr}$ values (S.D. = 1.06‰) is smaller than the marker size (Section S2). The error of individual $\Delta^{34}S_{CAS-pyr}$ values is the propagated error from paired $\delta^{34}S_{CAS}$ and $\delta^{34}S_{pyr}$ values (Section S2). Abbreviations: Sm. = Smithian, SSB = Smithian-Spathian boundary.

at the Environmental Analytical Facility of the School for the Environment at the University of Massachusetts Boston.

4.1. Carbonate-associated sulfate and pyrite extractions

We used the extraction protocol of Wotte et al. (2012) to extract carbonate-associated-sulfate. We leached between 75 and 150 g of powdered whole-rock sample, except sample 9–9 at 48 g, with 10% NaCl for 24-h intervals. This dissolved any NaCl-soluble sulfate. We precipitated the NaCl-soluble sulfate as BaSO₄ by adding 10% BaCl₂ solution. We repeated this leaching step until no further precipitation of BaSO₄ occurred. Subsequently, we dissolved the samples with 25% HCl until the reaction was complete. We precipitated any sulfate released during carbonate dissolution as BaSO₄. We weighed the BaSO₄ precipitate to stoichiometrically calculate the CAS concentration as SO_4^{2-} .

Using a modified chromium reduction method (Canfield et al., 1986; Sullivan et al., 2000), we isolated chromium reducible sulfur from 3 g of whole-rock powder. We assume that all product from chromium reduction is pyrite. In short, we gently boiled the reaction for 1 h under continuous N_2 flow, and we trapped the product as ZnS using a zinc acetate solution. We converted the ZnS to Ag_2S by adding silver nitrate. We weighed the Ag_2S to stoichiometrically determine pyritic sulfur concentrations ($S_{\rm pyr}$).

4.2. Sulfur and oxygen isotope measurements

For sulfur-isotope analyses ($\delta^{34}S_{CAS}$ and $\delta^{34}S_{pyr}$), we weighed 0.3–0.4 mg of BaSO₄ or Ag₂S into tin capsules with five to ten times vanadium pentoxide to aid in combustion. We used a Costech Elemental Analyzer ECS 4010 paired to a Thermo Delta V+ Isotope Ratio Mass Spectrometer to measure the isotopic compositions. We expressed the isotopic compositions in per mille notation (‰) relative to Vienna Canyon Diablo Troilite (VCDT). We ran isotopic standards every 12 unknown samples to correct $\delta^{34}S_{CAS}$ and $\delta^{34}S_{pyr}$ values to the VCDT reference scale. We used the BaSO₄ standards, IAEA-SO-5 (+0.49‰),

IAEA-SO-6 (-34.05%), and NBS-127 (+21.1%), and a check standard, IA-R025 (+8.53%), to determine the scale calibrated $\delta^{34}S$ values of each BaSO₄ unknown sample. We determined the precision, on average across all runs, to be < 0.35% based on replicate measurements of the IAEA and NBS standards. For each Ag₂S unknown sample, we used the Ag₂S standards, IAEA-S-1 (-0.3%), IAEA-S-2 (+22.67%), and IAEA-S-3 (-32.55%), and a BaSO₄ check standard, NBS-127 (+21.1%), to determine the scale calibrated $\delta^{34}S$ values. We determined the precision, on average across all runs, to be < 0.25% based on replicate measurements of the IAEA standards. We calculated the $\Delta^{34}S_{\text{CAS-pyr}}$ values as the difference between paired $\delta^{34}S_{\text{CAS}}$ and $\delta^{34}S_{\text{pyr}}$ values. We measured eight samples (12-6, 13-1, 13-2, 13-5, 13-7, 14-2, 14-5, and 14-6) in triplicate to estimate the heterogeneity of the CAS and pyrite extraction products for $\delta^{34}S$ values (Section S2; note: "S" indicates material in the Supplemental file).

For oxygen-isotope measurements of CAS ($\delta^{18}O_{CAS}$), we weighed 0.3–0.4 mg of BaSO₄ into silver capsules. We measured the isotope ratios using a Thermo Scientific TC/EA connected to a Thermo Delta V + Isotope Ratio Mass Spectrometer. Instrument parameters included a reactor temperature of 1450 °C, a GC temperature of 80 °C, and a helium flow rate of 90 mL min ⁻¹. We expressed the isotope ratios in per mille relative to Vienna Mean Ocean Water (VSMOW). We used two IAEA BaSO₄ standards, IAEA-SO-5 (+12.13‰) and IAEA-SO-6 (-11.35‰), and a check standard, NBS-127 (+8.59‰), to determine the scale calibrated δ^{18} O values of each unknown sample. We determined the precision to be < 0.45‰ for δ^{18} O values based on replicate measurements of the IAEA standards.

4.3. Carbonate carbon and oxygen isotope measurements

Stable C and O isotopic compositions of carbonates were analyzed at the University of Kentucky Environmental Research Training Laboratory using a GasBench-II peripheral coupled to a DeltaPlusXP isotope ratio mass spectrometer. Samples (450 \pm 50 mg) were equilibrated at 40 °C for 24 h before analysis. Average precision for $\delta^{13}C$

(+1.95‰) and $\delta^{18}O$ (-2.2‰) of NBS-19 calcite standard was 0.05‰ and 0.05‰, respectively, for the entire dataset. Average precision for $\delta^{13}C$ and $\delta^{18}O$ of unknowns was 0.02‰ and 0.05‰, respectively. All results are reported in per mille notation (‰) relative to Vienna Pee Dee Belemnite (VPDB).

4.4. Carbonate elemental concentrations

To isolate trace elements only associated with the carbonate fraction of the rock samples, we digested 100 mg of powdered sample using trace grade 1 M acetic acid under constant agitation for 24 h (Nothdurft et al., 2004). We quantified elements (Mg, Ca, Sr, Mn, and Al) on a Perkin Elmer Optima 3000 XL Inductively Coupled Plasma Optical Emission Spectrometer. We completely digested the carbonate standards NIST 1d limestone and NIST 88b dolomitic limestone using a sequential acid sequence of 3 to 1 HNO₃ to HF, 3 to 1 H₂O₂ to HNO₃, and just HNO3. We used a three-point serial dilution of the NIST 1d standard to calibrate unknown samples, and a 10 times dilution of NIST 88b as a check standard. Standards and blanks were run every 10 unknown samples. We measured each sample in triplicate with relative standard deviations (RSD) generally within 5%. The check standard values were within 5% difference of known values for all elements. Furthermore, we extracted the same sample five times to assess the method's reproducibility (Section S2). For another method test, we digested a subset of samples and standards using 1 M HCl to test the reproducibility of different acids (Section S2).

4.5. Carbon concentrations

Carbon concentrations were measured using an Eltra 2000C—S analyzer at the Department of Geology of the University of Cincinnati. Data quality was monitored via multiple analyses of USGS SDO-1 standard, yielding an analytical precision (2o) of \pm 2.5% of reported values. An aliquot of each sample was digested in 2 N HCl at 50 °C for 12 h to dissolve carbonate minerals, and the residue was analyzed for organic carbon ($C_{\rm org}$). The concentrations of total inorganic carbon were determined by difference.

4.6. Pyrite morphology

Using the HCl insoluble residues remaining after the CAS extraction, we examined pyrite morphology on a JEOL JSM-6010LA IntouchScope Scanning Electron Microscope in back scatter electron mode. We estimated the relative abundance of framboidal and euhedral pyrite within each sample, and used energy dispersive spectrometry to determine any significant $S_{\rm pyr}$ loss due to subaerial oxidative weathering.

5. Results

The mean total inorganic carbon concentration is $12.1 \pm 0.5\%$, C_{org} is 0.14 \pm 0.03%, and whole-rock Al concentration is $0.60 \pm 0.18\%$. All three analytes show little variation suggesting very pure carbonate throughout the section. The carbonate component elemental concentrations from the 1 M acetic acid digestion were highly reproducible and vielded similar results to the 1 M HCl digestions (Section S2). Carbonate Mg/(Mg + Ca) molar ratios range from 0.02 to 0.46. Carbonate component Mn/Sr molar ratios are mostly less than one except for three samples that are less than two. Carbonate Al concentrations are much lower compared to the whole-rock values and range from 64 to 499 ppm. A significant relation (Spearman's rho; r) exists between the whole-rock and acetic acid Al values (r = +0.65; p < 0.001). Using Al as a proxy for clay suggests that samples with higher whole-rock Al concentrations were more likely to contaminate the digestion for the carbonate component. However, differences in carbonate Al concentrations, used as a proxy for clay contamination, did not systematically affect measured Sr or Mn concentrations $(r \le \pm 0.26; p \ge 0.09)$ but did affect Ca (r = -0.42; p = 0.005) and Mg values (r = +0.30; p = 0.047).

The carbonate-carbon ($\delta^{13}C_{carb}$), CAS ($\delta^{34}S_{CAS}$ and $\delta^{18}O_{CAS}$), and pyrite $(\delta^{34}S_{pyr})$ isotope profiles record very similar and clearly defined long-term trends (Fig. 5). The variability in all three isotope profiles is much larger above 10 m. In all four isotope profiles, values generally increased from the base of the section until a max at about 10 m before broadly decreasing for the remainder of the sampled section (Fig. 5). $\delta^{13}C_{carb}$ values generally increased from about 0 to +3.6% before decreasing to values around +1%. A positive correlation exists between $\delta^{13}C_{carb}$ and $\delta^{18}O_{carb}$ values for all carbonate samples (r = +0.70; p < 0.001; Fig. S1A). $\delta^{34}S_{CAS}$ values range by about 21% with values increasing from about +30% to +39% before decreasing to +30% again. $\delta^{18}O_{CAS}$ values range by about 4% and increased from about +21% to +24% before decreasing to +21%. $\delta^{34}S_{pvr}$ values exhibit a range of about 17‰. $\delta^{34}S_{pyr}$ values increased from about +5to +10% to about +20% before broadly decreasing to about +5%. $\delta^{34}S_{CAS}$ values correlate significantly with both $\delta^{18}O_{CAS}$ values (r = +0.64; p < .001; Fig. S1D) and $\delta^{34}S_{pvr}$ values (r = +0.46; p < .001; Fig. S1D)p = 0.002). $\delta^{34}S_{CAS}$ values do not correlate with whole-rock Al concentrations (r = -0.04; p = 0.80; Fig. S1B). As the trends in δ^{34} S_{pvr} and $\delta^{34}S_{CAS}$ are similar, this led to a fairly stable $\Delta^{34}S_{CAS-pyr}$ profile. Δ^{34} S_{CAS-pyr} values range from 14.2 to 33.4% (mean of 24.9 \pm 3.9%). For the eight samples we measured in triplicate for $\delta^{34}S$ values, the average standard deviation was 1.06%, 1.23%, and 1.77% for $\delta^{34}S_{pyr}$, $\delta^{34}S_{CAS}$, and $\Delta^{34}S_{CAS-pyr}$ respectively (Section S2). We use these errors to estimate the per mille error of each individual sample. CAS concentrations range from 10 to 1063 ppm, and $S_{\rm pyr}$ concentrations range from 184 to 665 ppm. Lastly, we found only rare occurrences of euhedral pyrite, if any, within the Jesmond samples, and there were no signs of pyritic sulfur loss due to oxidative weathering.

6. Discussion

6.1. Screening and evaluation of primary origin of CAS signal

Our goal is to reconstruct as closely as possible the original CAS isotope pattern recorded at Jesmond. However, since CAS values at a given site can be shifted from the contemporaneous global mean and/or altered diagenetically (e.g., Present et al., 2015), it is important to assess if a given study section potentially records original, global values and screen for any altered values beyond sample-to-sample variability that may not reflect the global pattern. Altered CAS values may result from local environmental overprints, post-depositional alteration, or contamination from reduced sulfur sources during analytical extraction.

6.1.1. Screening of individual Jesmond samples

We began by identifying and screening out six samples whose isotopic compositions are likely to have been altered from their original values (12-3, 12-4, 16-5B2, and 16-9), or which may represent a local event (2-4 and 2-6). To identify altered samples, we used Grubbs' outlier test (Grubbs, 1950; Grubbs, 1969). The Grubbs' test considers the dataset as a whole, taking into account the difference between each sample and the mean value of the dataset as well as the variability within the dataset. Therefore, Grubb's outlier test identifies extreme values that exceed random sample-to-sample variability in the dataset. We did not specifically test the CAS isotope values but, rather, other diagnostic variables (pyr/CAS and $\delta^{18}{\rm O}_{\rm carb}$) that can indicate potential alteration of samples. This procedure helped to identify and screen out samples that do not preserve the original, global CAS pattern at Jesmond (Fig. 5). The reasons for removal were:

(1) Sano et al. (2012) described a calcareous shale bed in the lower unit as "an exceptional facies within the carbonate rocks of the Jesmond succession" and suggested that it may represent a subaerial exposure surface. Additionally, rapid and short-term fluctuations in

- $\delta^{13}C_{carb}$, especially when paired with sharp lithologic changes, likely do not mimic the global pattern (e.g., Schobben et al., 2016b). We interpret the rapid negative excursion in $\delta^{13}C_{carb}$ values within the calcareous shale (13.5 to 15 m) as a local signal (Fig. S2). This interval contains three samples (2-4, 2-5, and 2-6), two of which (2-4, 2-6) were extracted for CAS and pyrite.
- (2) We used a CAS extraction process optimized to reduce pyrite oxidation during the carbonate dissolution steps (Wotte et al., 2012). However, samples that record low CAS concentrations relative to pyrite (pyr/CAS ratios) are inherently more susceptible to $\delta^{34}S_{CAS}$ alteration due to pyrite oxidation (Schobben et al., 2015). We used Grubbs' outlier test to identify outliers in the pyr/CAS ratios. The Grubb's test identified samples 16-9 (pvr/CAS = 12.52. Zscore = 5.138, p-value < 0.01) and 12-4 (pyr/CAS = 5.38, Zscore = 1.729, p-value < 0.05) as outliers with high pyr/CAS values. The pyrite concentrations for both samples are close to the average for the entire section (~300-350 ppm), but their CAS concentrations are extremely low (28 and 56 ppm) compared to the rest of the section (100-1000 ppm). Thus, the high pyr/CAS ratios of these two unique samples are due to low CAS concentrations. The $\delta^{34}S_{CAS}$ values of both samples are ^{32}S -enriched by > 7% compared to their nearest neighbors (Figs. 5 and S1C). The low CAS concentrations of these samples may have failed to buffered them against $\delta^{34}S$ shifts due to oxidation of minor amounts of pyrite during the CAS extraction process. Alternatively, their low CAS concentrations may have allowed an unidentified local/diagenetic process to alter the isotopic compositions of these samples. In either case, their $\delta^{34}S_{CAS}$ values are unlikely to reflect a global signal. δ18O_{CAS} values can help identify contamination during the extraction process since any reduced sulfur species that are oxidized gain most of their oxygen from the laboratory water (Witts et al., 2018). The $\delta^{18}O_{CAS}$ value of sample 16–9 is the lowest of the entire section, but we do not know the $\delta^{18}O_{CAS}$ of the laboratory water to confirm this as direct evidence for contamination. The low CAS concentration of sample 12–4 did not allow measurement of $\delta^{18}O_{CAS}$.
- (3) A few Jesmond samples record anomalously low $\delta^{18}O_{carb}$ values, ranging from -7 to -14%, versus from -2 to -5% for other samples (Fig. S1A). We used Grubbs' outlier test to identify outliers in the $\delta^{18}O_{carb}$ dataset. The Grubb's test identified samples 13-3 and 12-2 (p-value < 0.05) and samples 16-5B2, 12-3, 8-5, and 6-1 (p-value < 0.01) as outliers. These anomalously low $\delta^{18}O_{carb}$ values likely reflect post-depositional alteration. We extracted two of these samples (12–3 and 16-5B2) for CAS and pyrite isotope values.

6.1.2. Evaluation of primary origin of CAS signal

Whole-rock $\delta^{34}S_{CAS}$ values are generally not strongly affected by factors such as meteoric diagenesis (Gill et al., 2008), early marine diagenesis (Lyons et al., 2004), sedimentation rates (Rennie and Turchyn, 2014), carbonate recrystallization rates (Rennie and Turchyn, 2014), and burial temperatures (Fichtner et al., 2017). From these studies, it seems that these processes create sample variability in $\delta^{34}S_{CAS}$ of ~4% relative to seawater sulfate $\delta^{34}S$. However, other case studies suggested dolomitization by incorporating continental weathering products (Marenco et al., 2008) or early diagenetic MSR (Present et al., 2015) can alter $\delta^{34}S_{CAS}$ by 9 to 15% relative to coeval $\delta^{34}S$ seawater and overprint the original marine signal. Based on high Mg/ (Ca + Mg) ratios of ~0.4 for the unscreened samples, it is clear that dolomitization affected the Jesmond samples. However, the incorporation of substantial continentally derived sulfur is not a concern for Jesmond due to its mid-Panthalassa paleolocation and lack of terrigenous clastic material (Sano et al., 2012). Furthermore, using wholerock Al concentrations as a proxy for clay material, there is no significant relationship between the unscreened whole-rock Al concentrations and $\delta^{34}S_{CAS}$ (r = -0.21; p = 0.20). However, a positive correlation between $\delta^{13}C_{carb}$ and $\delta^{18}O_{carb}$ for unscreened samples (r = +0.56; p < 0.001) may indicate some meteoric influence (e.g.,

Knauth and Kennedy, 2009). Since the Jesmond $\delta^{13}C_{carb}$ pattern matches the global $\delta^{13}C_{carb}$ long-term trend through the Smithian-Spathian transition (e.g., Song et al., 2013), the potential meteoric influence cannot have completely overprinted the original marine carbonate signals. CAS-isotope values can also potentially be buffered against the effects of meteoric diagenesis (Gill et al., 2008). Furthermore, the parallel trends in $\delta^{13}C_{carb}$ and $\delta^{34}S_{CAS}$ at Jesmond (Fig. 5) have also been reported from Lower Triassic sections in South China (Song et al., 2014) and thus may be indicative of contemporaneous global changes in seawater chemistry.

Carbonate recrystallization processes that occur at burial temperatures higher than 100 °C can increase $\delta^{18}O_{CAS}$ by up to 6% (Fichtner et al., 2017). These same processes do not alter $\delta^{34}S_{CAS}$. High carbonate Mn/Sr ratios can be used as a proxy for burial diagenesis and recrystallization of the carbonate lattice (e.g., Brand, 2004). Molar ratios less than one suggest data likely reflect original seawater chemistry (Brand, 2004). Only two samples at Jesmond (2-1 and 8-1) yielded Mn/ Sr ratios > 1 and these values are still < 2. The Mn/Sr data are consistent with limited alteration of the Jesmond samples. The degree of diagenetic alteration of carbonates correlates somewhat with burial temperatures, for which conodont color alteration index (CAI) is a proxy (Epstein et al., 1977). CAI values were not measured in this study, but the typical values for the Triassic of the Cache Creek Terrane are between 4 and 5, suggesting burial temperatures between 200 and 300 °C (Orchard, 1984). These burial temperatures may have shifted Jesmond samples to higher $\delta^{18}O_{\text{CAS}}$ values relative to the original seawater sulfate (Fichtner et al., 2017). The range of $\delta^{18}O_{CAS}$ at Jesseawater sulfate (Fichtner et al., 2017). mond (+20.3 to +23.9%) is comparable to lowermost Triassic sections in Iran (+21 to +25%; Schobben et al., 2015). The Iranian sections record CAI values between 1 and 1.5, corresponding to burial temperatures below the 100 °C threshold (Schobben et al., 2014). The similar $\delta^{18}O_{CAS}$ ranges of the Jesmond and Iranian sections suggest that Jesmond $\delta^{18}O_{CAS}$ data have not been significantly altered from their original marine sulfate values.

Comparing $\delta^{34}S_{CAS}$ with contemporaneous evaporite $\delta^{34}S$ values can help decipher if the absolute $\delta^{34}S_{CAS}$ values are reasonable. For example, $\delta^{34}S_{CAS}$ values from three different PTB sections (Newton et al., 2004; Song et al., 2014; Schobben et al., 2015) were found to be mostly $^{34}S_{cas}$ repriched compared to coeval $\delta^{34}S_{caporite}$ values (Bernasconi et al., 2017). Few temporally constrained evaporite deposits dating to the SSB have been reported (e.g., Bernasconi et al., 2017), although there is substantial low-resolution data for the Smithian and Spathian substages. Late Smithian evaporites record $\delta^{34}S$ of ca. +32‰, and Spathian samples yield $\delta^{34}S$ of ca. +27 to +35‰ (Holser, 1984; Marenco, 2007; Horacek et al., 2010; Bernasconi et al., 2017). The $\delta^{34}S_{CAS}$ record for Jesmond, with values mostly between +30 to +39‰, is thus consistent with the evaporite data.

In summary, the Jesmond CAS dataset appears to show, at most, limited modification of its primary marine $\delta^{34}S$ signature and, thus, is likely to record global seawater sulfate $\delta^{34}S$ trends during the Smithian-Spathian transition. Some influence of local MSR (Present et al., 2015, Fitchtner et al., 2017) cannot be ruled out at this time and may have contributed to the sample-to-sample variability in the Jesmond section. This variability would have been driven by different degrees of local MSR and/or different capacities of individual samples to buffer against alteration. However, the similarity of the Jesmond whole-rock $\delta^{34}S_{\text{CAS}}$ data to coeval $\delta^{34}S_{\text{evaporite}}$ records suggests that local MSR did not completely overprint the original values. However, trends in our dataset are probably more reliably interpreted than the absolute CAS isotope values.

6.2. Secular variation in seawater sulfate

6.2.1. A global or local signal at Jesmond?

Redox conditions during deposition of the Jesmond section were consistently oxic based on both petrographic and geochemical proxies

(Sano et al., 2012). Scarce fossils of small microgastropods, bivalves, ostracods, and crinoids were found scattered throughout the section along with limited vertical burrows. Sano et al. (2012) inferred stressed environmental conditions in a peritidal setting but not a lack of oxygen availability. The overall lack of pyrite framboids and limited euhedral pyrite found in this study provides secondary evidence for oxic deposition (e.g., Bond and Wignall, 2010), consistent with previous conclusions (Sano et al., 2012). From sections in Japan, the deep waters of the mid-Panthalassa were likely dysoxic to anoxic during the Smithian and early to middle Spathian (Isozaki, 1997; Wignall et al., 2010). However, the deeper oxygen-depleted mid-Panthalassic waters did not penetrate the ocean-surface layer, in which the Jesmond section accumulated, and therefore, were unlikely to overprint potential global CAS values with a local redox signal. A general lack of variation in $\Delta^{34}S_{CAS}$ pyr also suggests that the sulfur system did not respond to local organic matter availability. This factor would likely alter $\Delta^{34}S_{CAS-pvr}$, which can be used as a proxy for the apparent depletion during MSR. Furthermore, we can rule out substantial local changes in continental weathering based on the paleo-location within the mid-Panthalassa and a lack of coarse terrigenous grains (Sano et al., 2012). This leads us to conclude that $\delta^{34}S_{CAS}$ and $\delta^{18}O_{CAS}$ values were potentially responding to larger scale regional to global changes in sulfur cycling, but the most compelling evidence of a global signal is a comparison of δ^{34} S and δ^{18} O values and trends from other locations.

Based on comparisons with CAS profiles from two other areas (southern Neo-Tethys and eastern Paleo-Tethys; Fig. 3B) and available $\delta^{34}S_{evaporite}$ data, we infer that the Jesmond isotopic profiles likely represent global signals for Early Triassic seawater (Fig. 6). The Shitouzhai section from the eastern Paleo-Tethys (South China) also spans the SSB, but the global $\delta^{34}S_{CAS}$ signal was likely overprinted by a local upwelling process (Zhang et al., 2015). Our goal is to reconstruct global signals, so we do not include the Shitouzhai data with the Lower Guandao section for South China. Through the global SSB positive CIE, the key feature at Jesmond and Spiti Valley was a concurrent increase in $\delta^{34}S_{CAS}$ values (Spiti Valley: from +28 to +35‰; and Jesmond: from +30 to +38‰; Fig. 6). A broad increase (+20–25 to +30‰; Fig. 6) can also be identified at Lower Guandao but with less confidence due to a gap in carbonate deposition and higher sample-to-sample variability. Subsequently, as $\delta^{13}C_{carb}$ began to decrease from the early

Spathian to the middle Spathian, $\delta^{34}S_{CAS}$ also decreased at Jesmond (+38 to about +30‰) and with less confidence on the exact timing of the decrease at Lower Guandao (+30 to about +25‰). Comparing the $\delta^{34}S_{CAS}$ profiles of these three locations illustrates the inherent variability typical of whole-rock $\delta^{34}S_{CAS}$. This again highlights the need to focus on the overall pattern of change and not on sample-to-sample variation. Importantly, despite this variability, we can identify comparable trends at the different locales, e.g., at Spiti Valley and Jesmond and, with less confidence, at Lower Guandao, that reflect a global $\delta^{34}S_{CAS}$ signal (Fig. 6).

Further confidence that $\delta^{34}S_{CAS}$ likely represents a global signal is the similarity to the available $\delta^{34}S_{evaporite}$ data. The substage evaporite record broadly identified a late Early Triassic peak in $\delta^{34}S$ around the SSB (Bernasconi et al., 2017, and references therein). This provides confidence that the peak defined by $\delta^{34}S_{CAS}$ at the SSB, concurrent with the global $\delta^{13}C_{carb}$ peak, represents the most likely global $\delta^{34}S$ pattern to date for the SSB (Fig. 6). This shifts the likely relative $\delta^{34}S$ maximum of the late Early Triassic to a younger age within the earliest Spathian. More CAS and evaporite isotope data from other locations are still necessary to identify the global signals with complete confidence.

Secondary evidence of a global pattern recorded in CAS are the similarities between $\delta^{34} S_{CAS}$ and $\delta^{18} O_{CAS}$ at Spiti Valley and Jesmond (Fig. 6). For both sections there is a statistically significant and positive correlation between $\delta^{34} S_{CAS}$ and $\delta^{18} O_{CAS}$ (Jesmond: unscreened samples: $r=+0.61;\ p<0.001;\ Fig. S1D;\ Spiti Valley: <math display="inline">r=+0.44;\ p=0.029).$ In terms of absolute values of $\delta^{18} O_{CAS}$, the $\delta^{18} O_{CAS}$ values of Spiti Valley through the SSB transition vary around +20%, which agrees with the values at the start of the $\delta^{18} O_{CAS}$ increase at Jesmond (Fig. 6). There is no $\delta^{18} O_{evaporite}$ data bracketing the SSB available for comparison that we know of. Lastly, there is a clear increase in $\delta^{18} O_{CAS}$ across the SSB at Jesmond, but the increased variability within the SSB interval at Spiti Valley makes the trend there less distinct. However, at a minimum, $\delta^{18} O_{CAS}$ values within the SSB transition at Spiti Valley were higher than late Smithian values.

While multiple sections globally exhibit similar trends in $\delta^{34}S_{CAS}$ across the SSB, there are significant differences in their absolute values. Local or regional variation in isotopic signals was not unique to the SSB, as it also occurred, for example, around the PTB (Newton et al., 2004; Song et al., 2014; Schobben et al., 2015; Bernasconi et al., 2017). The

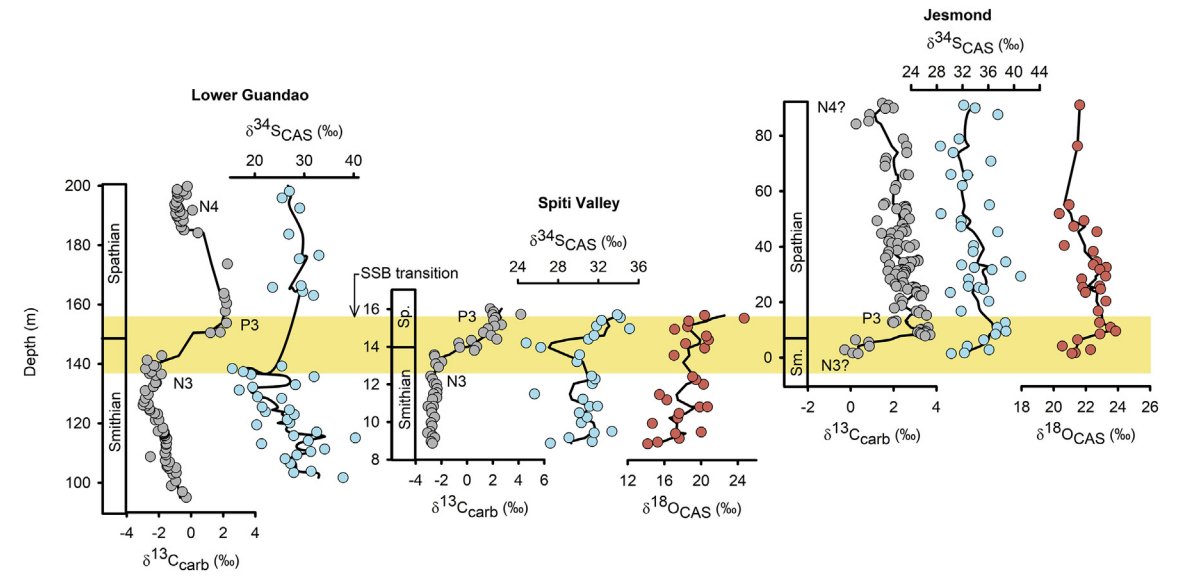


Fig. 6. Comparisons of $\delta^{13}C_{carb}$, $\delta^{34}S_{CAS}$, and $\delta^{18}O_{CAS}$ between globally distributed sections. The bar marks the SSB positive carbon isotope excursion at each section. The N3, P3, and N4 nomenclature follows Song et al. (2013); "?" indicates uncertainty whether the C-isotope minima at the base and top of the section are the true N3 and N4 minima. The solid lines are five-point moving averages for $\delta^{13}C_{carb}$ and three-point moving averages for $\delta^{34}S_{CAS}$ and $\delta^{18}O_{CAS}$. Data for Lower Guandao from previously published papers (Payne et al., 2004; Song et al., 2014) and Spiti Valley from Stebbins (2018) and Stebbins et al. (2018). Screened samples for Jesmond (Section 6.1.1) are not included. Abbreviations: Sm. – Smithian and Sp. – Spathian.

differences between the SSB sections are likely due to locally variable diagenetic overprints altering δ^{34} S from the global value (Present et al., 2015; Fichtner et al., 2017) or depositional conditions, such as redox or organic matter availability (e.g., Schobben et al., 2017). Some local $\delta^{34}S$ variability is to be expected based on measurements of $\delta^{34}S$ of modern seawater sulfate from globally distributed unrestricted-biogenic sediments (opal and carbonate ooze; Schobben et al., 2017, and references therein). This compilation of modern data suggested that sulfate sources (aqueous porewaters, CAS, barite) within unrestrictedbiogenic sediments exhibit a standard deviation of ± 2.73% around the modern seawater sulfate δ^{34} S value (n = 141 measurements). Assuming a similar amount of local variability for the SSB explains some proportion of the differences in absolute $\delta^{34}S_{CAS}$ between sites. If differences in absolute CAS values are eventually proven to be a primary signal, instead of due to diagenetic alteration, then local variation was likely related to low seawater sulfate concentrations at the SSB (2.5 to 9.1 mM; Section 6.3) as well as in older Early Triassic substages (0.6 to 6 mM; Luo et al., 2010; Song et al., 2014; Bernasconi et al., 2017; Schobben et al., 2017). Low marine sulfate concentrations would have permitted greater regional heterogeniety in seawater sulfate isotopic compositions between watermasses, as proposed for the Early Jurassic when seawater sulfate concentrations were ~1-5 mM (Newton et al., 2011). Overall, more work is necessary to decipher exactly what caused the differences in absolute $\delta^{34}S_{\text{CAS}}$ between sections and whether they are offset from contemporaneous $\delta^{34}S_{\text{eavporite}}$ but, importantly, the long-term trends in these sections are similar.

6.2.2. Paleoenvironmental drivers of secular variation

The nature of changes in global marine environmental conditions across the SSB can be inferred from the Jesmond CAS records. The strong relationship between $\delta^{34}S_{CAS}$ and $\delta^{18}O_{CAS}$ at Jesmond (unscreened samples: r = +0.61; p < 0.001; Fig. S1D) limits the type of global driver that controlled CAS-isotope variation. This covariation is also recorded at Spiti Valley around the SSB (r = +0.44; p = 0.029; Stebbins, 2018; Stebbins et al., 2018). Two possible global drivers were variation in riverine sulfate inputs due to volcanism or weathering, and variation in the net MSR rates and net pyrite burial fluxes. Both riverine sulfate inputs are typically 32 S- and 16 O-enriched compared to the marine sulfate pool, which is 34 S- and 18 O-enriched owing to MSR and pyrite burial (e.g., Bottrell and Newton, 2006; Fig. 2). Therefore, the riverine source flux and pyrite sink flux change the isotope values of seawater sulfate in opposite ways, but changes in either flux can generate covariation between $\delta^{34}S$ and $\delta^{18}O$. However, the change riverine source or pyrite sink flux must have been temporary to account for the peaks in the isotope profiles.

Either global volcanic or weathering inputs can cause a relative decrease in $\delta^{34}S_{CAS}$ and $\delta^{18}O_{CAS}.$ In theory, cyclical decreases in the amount of volcanism or weathering may account for the SSB peak in $\delta^{34}S_{CAS}$ and $\delta^{18}O_{CAS}.$ Volcanism is potentially a logical driver based on temperature reconstructions that suggest a transient cooling interval around the SSB (Sun et al., 2012; Romano et al., 2013). Mercury concentrations in NW Pangea from shale and siltstones suggest a pulse of volcanism occurred from the late Smithian CIE minimum through the SSB positive CIE (Grasby et al., 2013b, 2015; Shen et al., in review). The high concentrations of mercury recorded in the latest Smithian would link volcanism to the lower $\delta^{34}S_{CAS}$ and $\delta^{18}O_{CAS}$ during this interval. However, mercury concentrations did not increase after the SSB positive CIE when $\delta^{34}S_{CAS}$ and $\delta^{18}O_{CAS}$ values decreased again. An alternative view using U—Pb dating suggests the majority of Siberian Traps volcanism ended well prior to the SSB (Burgess and Bowring, 2015). Both views suggest volcanism was not the primary control on the CASisotope trends. Similarly, for global weathering fluxes, modeling of changes from the Zal, Iran section suggests there was a single drastic decrease across the SSB (Sedlacek et al., 2014). No subsequent increase is recorded again in the early to middle Spathian to reflect the cyclical nature of the CAS-isotope peak. On the other hand, Sr isotopes at South China suggests there was a small peak in weathering, but the increase was coeval with the SSB positive CIE (Song et al., 2015). This is opposite of the expected result.

CAS-isotope trends were most likely the result of the net flux of MSR and pyrite burial. Decreases in the net MSR flux and pyrite burial leads to a decrease in $\delta^{34}S_{CAS}$ and $\delta^{18}O_{CAS}$ values and vice versa (e.g., Bottrell and Newton, 2006). Our data suggest that the net MSR flux and pyrite burial increased across the SSB concomitant with the positive CIE. A scenario linked to $\delta^{13} C_{\text{carb}}$ which reflect increased primary productivity and weakened ocean stratification (Song et al., 2013). The decrease in temperatures across the SSB likely started the chain of events (Sun et al., 2012; Romano et al., 2013). Cooling temperatures across the SSB resulted in weakened oceanic stratification, increased cycling of nutrients to stimulate productivity, and increased availability of organic matter to facilitate the net increase in MSR and pyrite burial. Song et al. (2014) suggested this chain of events for the majority of the Early Triassic, but the SSB may have been unique (e.g., Zhang et al., 2015). The data from Jesmond proposes that the SSB to early Spathian also experienced the environmental scenario suggested for the majority of the Early Triassic. This environmental scenario advocates that more MSR occurred when marine biota recovered (Stanley, 2009; Brayard et al., 2017; Foster et al., 2017, and references therein), a scenario also noted for the initial recovery interval following the end-Cretaceous extinction event (Witts et al., 2018). Although the SSB ocean was still much hotter than prior to the end-Permian mass extinction (Sun et al., 2012), the slight decrease from the extremes of the late Smithian may have facilitated the recovery interval across the SSB.

During the early to middle Spathian global signals in CAS isotopes, $8^{13}C_{carb}$ (e.g., Song et al., 2013), and other environmental variables like temperature and oxygenation (e.g., Sun et al., 2012; Grasby et al., 2013a) returned toward late Smithian values. The late Smithian experienced a crisis for conodonts, ammonoids, and some benthic communities (Brayard et al., 2006; Orchard, 2007; Stanley, 2009; Hofmann et al., 2014), and the trend back toward these values suggests potential for a similar crisis. Furthermore, evidence for a middle to late Spathian crisis exists for conodonts and ammonoids (Stanley, 2009). In this sense, the SSB did not mark a unique time interval as it was one of the many transient recovery periods and sulfur cycle perturbations during the Early Triassic (Stanley, 2009; Song et al., 2014).

6.3. Seawater sulfate concentrations during the SSB

The quantitative reconstruction of seawater sulfate and changes over time furthers our understanding of Earth's past seawater chemistry (Kah et al., 2004; Algeo et al., 2015). Algeo et al. (2015) provided two methods to quantitatively reconstruct paleo-seawater sulfate: (1) the MSR-trend method and (2) the rate method. The MSR-trend method relies on the relation between the isotope depletion due to MSR and seawater sulfate concentrations (Fig. 7), and the rate method relies on seawater sulfate δ^{34} S variation. Importantly, the rate of change method provides a maximum estimate of seawater sulfate concentrations while the MSR-trend method produces a mean estimate (Algeo et al., 2015).

The $\Delta^{34}S_{CAS-pyr}$ values can be used as a proxy for the isotope depletion due to MSR in order to use the MSR-trend method for paleoenvironmental studies. The Jesmond $\Delta^{34}S_{CAS-pyr}$ recorded no overall change across the SSB (Fig. 5D). We can rule out a $\Delta^{34}S_{CAS-pyr}$ control by temperature as this changed across the SSB (Sun et al., 2012; Romano et al., 2013). The paleolocation of Jesmond rules out any substantial local effects due to continental weathering and local redox conditions remained consistently oxic (Sano et al., 2012). The lack of $\Delta^{34}S_{CAS-pyr}$ change also suggests that local MSR and pyrite deposition occurred under relatively uniform conditions and did not vary between openand closed-system conditions. Ruling out these drivers suggests that $\Delta^{34}S_{CAS-pyr}$ likely reflects the apparent depletion due to MSR. Jesmond is therefore a strong candidate for the MSR-trend method to reconstruct SSB seawater sulfate concentrations (Algeo et al., 2015). Using a

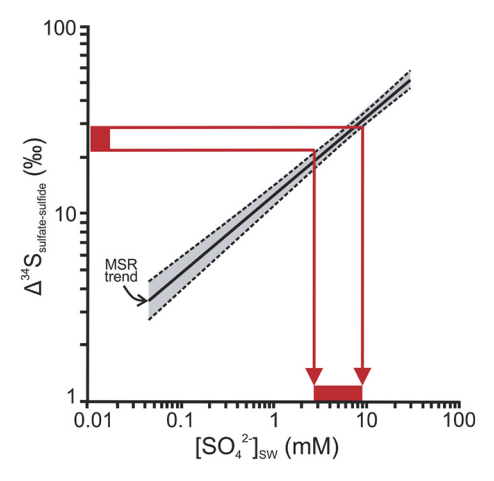


Fig. 7. Determination of SSB seawater sulfate concentrations (mM) using the MSR-trend method (Algeo et al., 2015). We use the relation between $\Delta^{34}S_{sulfate-sulfide}$ and $[SO_4{}^2^-]_{SW}$ (solid line) with confidence intervals (dashed lines) to calculate the mean and range of SSB sulfate concentrations based on the mean \pm standard deviation of measured $\Delta^{34}S_{CAS-DVI}$.

Jesmond mean $\Delta^{34}S_{CAS-pyr}$ value of 25.4 \pm 3.6‰ for unscreened samples, we produce a mean estimate of 5.0 mM with a range of 2.5 to 9.1 mM for the latest Smithian to early Spathian (Fig. 7). An important caveat, as noted for the Permian-Triassic boundary interval by Bernasconi et al. (2017), is potential $^{34}S_{\text{enrichment}}$ of CAS relative to the $\delta^{34}S$ of coeval seawater sulfate (as proxied by $\delta^{34}S_{\text{evaporite}}$). At the Permian-Triassic boundary, the $^{34}S_{\text{enrichment}}$ was around +5 to +10‰ (Bernasconi et al., 2017). Incorporating an offset between $\delta^{34}S_{CAS}$ and $\delta^{34}S_{\text{evaporite}}$ into the MSR-trend method would result in a lower estimate of seawater sulfate concentrations. However, based on available data to date, the $\delta^{34}S_{\text{evaporite}}$ values around the SSB broadly match the $\delta^{34}S_{CAS}$ of Jesmond (Section 6.1.2), so more $\delta^{34}S_{\text{evaporite}}$ data will be needed to evaluate any potential offset.

Invariant $\Delta^{34}S_{\text{CAS-pyr}}$ values through the SSB interval suggest that seawater sulfate concentrations did not change appreciably. However, an increase in pyrite burial rates probably accounted for the increase in $\delta^{34}S_{CAS}$ values across the SSB (see Section 6.2.2). We speculatively hypothesize two potential scenarios, but more work is needed to confirm either suggestion. First, higher pyrite burial rates would have been accompanied by a decrease in seawater sulfate concentrations to some degree if not countered by a change in sulfate input fluxes such as continental weathering. Possible sources include: (1) decreased evaporite formation, (2) increased volcanic sulfate inputs, or (3) increased weathering sulfate fluxes. Evaporite formation likely increased across the SSB due to a change from relatively more humid to drier climatic conditions based on spore to pollen ratios (Galfetti et al., 2007; Hermann et al., 2012). Furthermore, evidence for massive volcanism suggests that it peaked in the latest Smithian not across the SSB (Grasby et al., 2015; Shen et al., in review; Section 6.2.2). The likely source was a temporary increase in continental weathering across the SSB. Based on global modeling of Sr isotopes (Song et al., 2015) as well as a few studies based on local depositional conditions (e.g., Lehrmann et al., 2015), it is possible that a short-term increase in continental weathering occurred during the SSB and early Spathian. The likely mechanism leading to increased weathering around the SSB stemmed from the short-term cooling event (Sun et al., 2012; Romano et al., 2013) and a subsequent sea-level fall at the SSB (Snedden and Liu, 2010). Previously deposited but newly exposed fine-grained sediment would have been remobilized and pyrite oxidation rates would have spiked, increasing sulfate inputs to the marine sulfate pool. A similar mechanism has been used to explain features of the Pleistocene global sulfur record during glacial periods (Markovic et al., 2015). Alternatively, there may have been a short-term decrease in seawater sulfate concentrations at the SSB

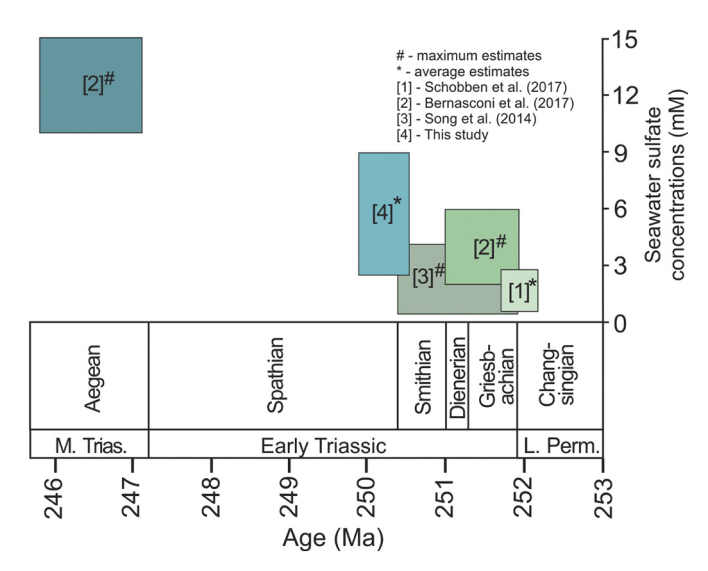


Fig. 8. Estimates of paleo-seawater sulfate concentrations for the PTB, Early Triassic, and the beginning of the Middle Triassic. The box edges mark the age range and concentration range for each study. Reconstructions are based on either the MSR-trend (average estimate; *) or rate method (maximum estimate; #) of Algeo et al. (2015). Data from: [1] - Schobben et al. (2017); [2] - Bernasconi et al. (2017); [3] - Song et al. (2014); [4] - this study. Abbreviation: M. Trias. – Middle Triassic, L. Perm. – Late Permian.

that has not been recognized owing to the limited stratigraphic resolution of the existing datasets.

Our estimate for mean seawater sulfate at the SSB (2.5 to 9.1 mM) can be compared to published values for the Permian-Triassic boundary (PTB) and Middle Triassic (Fig. 8). Using the same MSR-trend method, Schobben et al. (2017) estimated a range of 0.6 to 2.8 mM for the PTB in the western Paleo-Tethys. For a similar time interval, Luo et al. (2010) estimated < 1 mM based on the relationship between $\delta^{13}C_{carb}$ and $\delta^{34}S_{CAS}$ for the eastern Paleo-Tethys. Moving slightly younger into the Griesbachian through Smithian substages and using the rate method, Song et al. (2014) estimated a maximum concentration < 4.2 mM for the eastern Paleo-Tethys. Alternatively, using the rate method on evaporite δ^{34} S, Bernasconi et al. (2017) calculated a maximum range between 2 and 6 mM for the Griesbachian through Dienerian substages. Our conservative mean estimate from Jesmond in the mid-Panthalassa for the even younger SSB is higher than most of these estimates (Fig. 8). This suggests that through the course of the Early Triassic, there was a net increase in seawater sulfate. Following the SSB, the δ³⁴S values of Middle Triassic CAS and evaporites stabilized (Song et al., 2014; Bernasconi et al., 2017). The decreased rates of change suggest even further growth in the seawater sulfate pool during the Spathian and Middle Triassic. Maximum estimates following the SSB based on the rate method are between 10 and 15 mM (Bernasconi et al., 2017). Therefore, at the SSB, Jesmond recorded intermediate seawater sulfate between the low concentrations of the PTB and relatively higher concentrations of the Middle Triassic.

7. Conclusions

We draw the following conclusions from the carbon-sulfur isotope study of the mid-Panthalassa Jesmond section:

- (1) Based on the high-resolution $\delta^{13}C_{carb}$, the midpoint value of the positive CIE associated with the SSB occurred at 7.1 m. This constrains the highest possible stratigraphic location of the SSB at Jesmond. The new boundary location is slightly below the previously suggested location based on the conodont fossil record.
- (2) Both the $\delta^{34}S_{CAS}$ and $\delta^{18}O_{CAS}$ increased across the SSB at Jesmond.

- This increase occurred at the same time as the SSB positive CIE. A trend that occurred in $\delta^{34}S_{CAS}$ at two other locations suggesting a global signal. The environmental mechanism responsible for the increase in $\delta^{34}S_{CAS}$ and $\delta^{18}O_{CAS}$ was an increase in MSR and the net pyrite burial flux. The conditions associated with the marine sulfur cycle perturbation at the SSB were temporary as the excursions in $\delta^{34}S_{CAS}$ and $\delta^{18}O_{CAS}$ began to relax toward pre-perturbation values rapidly after the SSB.
- (3) We calculate a mean estimate of the seawater sulfate concentration for the SSB between 2.5 and 9.1 mM using the MSR-trend method. Sulfate concentration does not change measurably from the latest Smithian through the earliest Spathian. These values were intermediate to PTB and Middle Triassic values and suggest an overall growth in the sulfate pool through the Early Triassic.

Acknowledgments

We thank Dr. Michael Orchard for helpful discussions. The authors thank Dr. Ron Blakey for developing and allowing use of a new Early Triassic paleogeographic map. AS thanks the Environmental Analytical Facility at UMass Boston's School for the Environment (NSF Award # 09-42371; DBI:MRI-RI2; PIs: RH and Dr. Alan Christian) for access to analytical instrumentation. AS gratefully acknowledges support by the National Science Foundation Graduate Research Fellowship (DGE-1356104), UMass Boston Chancellor's Distinguished Doctoral Fellowship, and UMass Boston's School for the Environment. TJA thanks the Sedimentary Geology and Paleobiology program of the U.S. National Science Foundation, the NASA Exobiology program, and the China University of Geosciences-Wuhan (SKL-GPMR program GPMR201301, and SKL-BGEG program BGL21407) for research support. Thanks to Sylvain Richoz for editorial handling and to Stefano Bernasconi and Rob Newton for constructive reviews of the original manuscript.

Appendix A. Supplementary data

Supplementary data to this article can be found online at https://doi.org/10.1016/j.earscirev.2018.08.010.

References

- Aita, Y., Spörli, K., 2007. Geological framework for the pelagic Permian/Triassic oceanic sequence of Arrow Rocks, Waipapa terrane, Northland, New Zealand: the oceanic Permian/Triassic boundary sequence at Arrow Rocks (Oruatemanu), Northland, New Zealand. GNS Sci. Monogr. 24, 1–16.
- Algeo, T.J., Hinnov, L., Moser, J., Maynard, J.B., Elswick, E., Kuwahara, K., Sano, H., 2010. Changes in productivity and redox conditions in the Panthalassic Ocean during the latest Permian. Geology 38 (2), 187–190.
- Algeo, T.J., Kuwahara, K., Sano, H., Bates, S., Lyons, T., Elswick, E., Hinnov, L., Ellwood, B., Moser, J., Maynard, J.B., 2011. Spatial variation in sediment fluxes, redox conditions, and productivity in the Permian–Triassic Panthalassic Ocean: Palaeogeography, Palaeoclimatology. Palaeoecology 308 (1–2), 65–83.
- Algeo, T.J., Luo, G.M., Song, H.Y., Lyons, T.W., Canfield, D.E., 2015. Reconstruction of secular variation in seawater sulfate concentrations. Biogeosci. Discuss. 12 (7), 2131–2151.
- Bernasconi, S.M., Meier, I., Wohlwend, S., Brack, P., Hochuli, P.A., Bläsi, H., Wortmann, U.G., Ramseyer, K., 2017. An evaporite-based high-resolution sulfur isotope record of late Permian and Triassic seawater sulfate. Geochim. Cosmochim. Acta 204, 331–349.
- Beyers, J., Orchard, M., 1989. Permian–Triassic boundary beds in the Cache Creek group Marble Range, near Jesmond, British Columbia. Geol. Survey Can. 89, 127–132.
- Beyers, J., Orchard, M., 1991. Upper Permian and Triassic conodont faunas from the type area of the Cache Creek complex, south-Central British Columbia. Canada 417, 269–297.
- Bond, D.P.G., Wignall, P.B., 2010. Pyrite framboid study of marine Permian-Triassic boundary sections: a complex anoxic event and its relationship to contemporaneous mass extinction. Geol. Soc. Am. Bull. 122 (7–8), 1265–1279.
- Bottrell, S.H., Newton, R.J., 2006. Reconstruction of changes in global sulfur cycling from marine sulfate isotopes. Earth Sci. Rev. 75 (1–4), 59–83.
- Brand, U., 2004. Carbon, oxygen and strontium isotopes in Paleozoic carbonate components: an evaluation of original seawater-chemistry proxies. Chem. Geol. 204 (1–2), 23–44.
- Brayard, A., Bucher, H., Escarguel, G., Fluteau, F., Bourquin, S., Galfetti, T., 2006. The

- early Triassic ammonoid recovery: Paleoclimatic significance of diversity gradients. Palaeogeogr., Palaeoclimatol. Palaeoecol. 239 (3–4), 374–395.
- Brayard, A., Krumenacker, L.J., Botting, J.P., Jenks, J.F., Bylund, K.G., Fara, E., Vennin, E., Olivier, N., Goudemand, N., Saucede, T., Charbonnier, S., Romano, C., Doguzhaeva, L., Thuy, B., Hautmann, M., Stephen, D.A., Thomazo, C., Escarguel, G., 2017. Unexpected early Triassic marine ecosystem and the rise of the Modern evolutionary fauna. Sci. Adv. 3 (2), e1602159.
- Brühwiler, T., Bucher, H., Brayard, A., Goudemand, N., 2010. High-resolution biochronology and diversity dynamics of the early Triassic ammonoid recovery: the Smithian faunas of the Northern Indian margin. Palaeogeogr. Palaeoclimatol. Palaeoecol. 297 (2), 491–501.
- Brunner, B., Bernasconi, S.M., 2005. A revised isotope fractionation model for dissimilatory sulfate reduction in sulfate reducing bacteria. Geochim. Cosmochim. Acta 69 (20), 4759–4771.
- Brunner, B., Bernasconi, S.M., Kleikemper, J., Schroth, M.H., 2005. A model for oxygen and sulfur isotope fractionation in sulfate during bacterial sulfate reduction processes. Geochim. Cosmochim. Acta 69 (20), 4773–4785.
- Burgess, S.D., Bowring, S.A., 2015. High-precision geochronology confirms voluminous magmatism before, during, and after Earth's most severe extinction. Sci. Adv. 1 (7), e1500470.
- Burgess, S.D., Bowring, S., Shen, S.Z., 2014. High-precision timeline for Earth's most severe extinction. Proc. Natl. Acad. Sci. USA 111 (9), 3316–3321.
- Canfield, D.E., Raiswell, R., Westrich, J.T., Reaves, C.M., Berner, R.A., 1986. The use of chromium reduction in the analysis of reduced inorganic sulfur in sediments and shales. Chem. Geol. 54 (1–2), 149–155.
- Chambers, L.A., Trudinger, P.A., 1979. Microbiological fractionation of stable sulfur isotopes: a review and critique. Geomicrobiol J. 1 (3), 249–293.
- Chen, Y., Twitchett, R.J., Jiang, H., Richoz, S., Lai, X., Yan, C., Sun, Y., Liu, X., Wang, L., 2013. Size variation of conodonts during the Smithian–Spathian (Early Triassic) global warming event. Geology 41 (8), 823–826.
- Chen, Y., Jiang, H., Lai, X., Yan, C., Richoz, S., Liu, X., Wang, L., 2015. Early Triassic conodonts of Jiarong, Nanpanjiang Basin, southern Guizhou Province, South China. J. Asian Earth Sci. 105, 104–121.
- Clarkson, M.O., Wood, R.A., Poulton, S.W., Richoz, S., Newton, R.J., Kasemann, S.A., Bowyer, F., Krystyn, L., 2016. Dynamic anoxic ferruginous conditions during the end-Permian mass extinction and recovery. Nat. Commun. 7, 12236.
- Claypool, G.E., Holser, W.T., Kaplan, I.R., Sakai, H., Zak, I., 1980. The age curves of sulfur and oxygen isotopes in marine sulfate and their mutual interpretation. Chem. Geol. 28, 199–260.
- Corsetti, F.A., Baud, A., Marenco, P.J., Richoz, S., 2005. Summary of Early Triassic carbon isotone records. Comptes Rendus Palevol 4 (6–7), 473–486.
- Epstein, A.G., Epstein, J.B., Harris, L.D., 1977. Conodont Color Alteration: An Index to Organic Metamorphism. United States Geological Survey (Professional Paper 995).
- Fichtner, V., Strauss, H., Immenhauser, A., Buhl, D., Neuser, R.D., Niedermayr, A., 2017.

 Diagenesis of carbonate associated sulfate. Chem. Geol. 463. 61–75.
- Fike, D.A., Bradley, A.S., Rose, C.V., 2015. Rethinking the ancient sulfur cycle. Annu. Rev. Earth Planet. Sci. 43, 593–622.
- Foster, W.J., Danise, S., Price, G.D., Twitchett, R.J., 2017. Subsequent biotic crises delayed marine recovery following the late Permian mass extinction event in northern Italy. PLoS One 12 (3), e0172321.
- Fritz, P., Basharmal, G.M., Drimmie, R.J., Ibsen, J., Qureshi, R.M., 1989. Oxygen isotope exchange between sulphate and water during bacterial reduction of sulphate. Chem. Geol. 79 (2), 99–105.
- Galfetti, T., Hochuli, P.A., Brayard, A., Bucher, H., Weissert, H., Vigran, J.O., 2007.Smithian-Spathian boundary event: evidence for global climatic change in the wake of the end-Permian biotic crisis. Geology 35 (4), 291–294.
- Gill, B.C., Lyons, T.W., Frank, T.D., 2008. Behavior of carbonate-associated sulfate during meteoric diagenesis and implications for the sulfur isotope paleoproxy. Geochim. Cosmochim. Acta 72 (19), 4699–4711.
- Gomes, M.L., Hurtgen, M.T., 2015. Sulfur isotope fractionation in modern euxinic systems: Implications for paleoenvironmental reconstructions of paired sulfate-sulfide isotope records. Geochim. Cosmochim. Acta 157, 39–55.
- Gomes, M.L., Hurtgen, M.T., Sageman, B.B., 2016. Biogeochemical sulfur cycling during cretaceous oceanic anoxic events: a comparison of OAE1a and OAE2. Paleoceanography 31 (2), 233–251.
- Grasby, S.E., Beauchamp, B., Embry, A., Sanei, H., 2013a. Recurrent early Triassic Ocean anoxia. Geology 41 (2), 175–178.
- Grasby, S.E., Sanei, H., Beauchamp, B., Chen, Z., 2013b. Mercury deposition through the Permo-Triassic Biotic Crisis. Chem. Geol. 351, 209-216.
- Grasby, S.E., Beauchamp, B., Bond, D.P.G., Wignall, P.B., Sanei, H., 2015. Mercury anomalies associated with three extinction events (Capitanian Crisis, Latest Permian Extinction and the Smithian/Spathian Extinction) in NW Pangea. Geol. Mag. 153 (2), 285–297.
- Grubbs, F.E., 1950. Sample criteria for testing outlying observations. Ann. Math. Statist. 21 (1), 27–58.
- Grubbs, F.E., 1969. Procedures for detecting outlying observations in samples. Technometrics 11 (1), 1–21.
- Hermann, E., Hochuli, P.A., Bucher, H., Brühwiler, T., Hautmann, M., Ware, D., Weissert, H., Roohi, G., Yaseen, A., 2012. Climatic oscillations at the onset of the Mesozoic inferred from palynological records from the North Indian margin. J. Geol. Soc. 169, 227–237.
- Hochuli, P.A., Sanson-Barrera, A., Schneebeli-Hermann, E., Bucher, H., 2016. Severest crisis overlooked—Worst disruption of terrestrial environments postdates the Permian–Triassic mass extinction. Sci. Rep. 6, 28372.
- Hofmann, R., Hautmann, M., Brayard, A., Nützel, A., Bylund, K.G., Jenks, J.F., Vennin, E., Olivier, N., Bucher, H., 2014. Recovery of benthic marine communities from the end-

- Permian mass extinction at the low latitudes of eastern Panthalassa. Palaeontology 57 (3), 547–589.
- Holser, W.T., 1984. Gradual and abrupt shifts in ocean chemistry during phanerozoic time. In: Holland, H.D., Trendall, A.F. (Eds.), Patterns of Change in Earth Evolution:
 Report of the Dahlem Workshop Patterns of Change in Earth Evolution Berlin 1983,
 May 1–6. Springer Berlin Heidelberg, Berlin, Heidelberg, pp. 123–143.
- Horacek, M., Koike, T., Richoz, S., 2009. Lower Triassic δ^{13} C isotope curve from shallow-marine carbonates in Japan, Panthalassa realm: Confirmation of the Tethys δ^{13} C curve. J. Asian Earth Sci. 36 (6), 481–490.
- Horacek, M., Brandner, R., Richoz, S., Povoden-Karadeniz, E., 2010. Lower Triassic Sulphur isotope curve of marine sulphates from the Dolomites, N-Italy: Palaeogeography, Palaeoclimatology. Palaeoecology 290 (1–4), 65–70.
- Hori, R.S., Yamakita, S., Ikehara, M., Kodama, K., Aita, Y., Sakai, T., Takemura, A., Kamata, Y., Suzuki, N., Takahashi, S., Spörli, K.B., Grant-Mackie, J.A., 2011. Early Triassic (Induan) Radiolaria and carbon-isotope ratios of a deep-sea sequence from Waiheke Island, North Island. New Zealand: Palaeoworld 20 (2–3), 166–178.
- Huang, Y.G., Chen, Z.Q., Wignall, P.B., Zhao, L.S., 2017. Latest Permian to Middle Triassic redox condition variations in ramp settings, South China: Pyrite framboid evidence. Geol. Soc. Am. Bull. 129 (1–2), 229–243.
- Isozaki, Y., 1997. Permo-Triassic boundary superanoxia and stratified superocean: Records from lost deep sea. Science 276 (5310), 235–238.
- Isozaki, Y., 2009. Integrated "plume winter" scenario for the double-phased extinction during the Paleozoic-Mesozoic transition: the G-LB and P-TB events from a Panthalassan perspective. J. Asian Earth Sci. 36 (6), 459–480.
- Johnston, S.T., Borel, G.D., 2007. The odyssey of the Cache Creek terrane Canadian Cordillera: Implications for accretionary orogens, tectonic setting of Panthalassa, the Pacific superwell, and break-up of Pangea. Earth Planet. Sci. Lett. 253 (3–4), 415–428.
- Jorgensen, B.B., 1982. Mineralization of organic matter in the sea bed the role of sulphate reduction. Nature 296, 643–645.
- Kah, L.C., Lyons, T.W., Frank, T.D., 2004. Low marine sulphate and protracted oxygenation of the Proterozoic biosphere. Nature 431, 834–838.
- Kampschulte, A., Strauss, H., 1998. The isotopic composition of trace sulphates in Paleozoic biogenic carbonates: implications for coeval seawater and geochemical cycles. Mineral. Mag 62, 744–745.
- Kampschulte, A., Strauss, H., 2004. The sulfur isotopic evolution of Phanerozoic seawater based on the analysis of structurally substituted sulfate in carbonates. Chem. Geol. 204 (3–4), 255–286.
- Knauth, L.P., Kennedy, M.J., 2009. The late Precambrian greening of the Earth. Nature 460 (7256), 728–732.
- Kozur, H., 2003. Integrated Ammonoid, Conodont and radiolarian zonation of the Triassic and some remarks to stage/substage subdivision and the numeric age of the Triassic stages. Albertiana 28, 57–74.
- Kump, L.R., Pavlov, A., Arthur, M.A., 2005. Massive release of hydrogen sulfide to the surface ocean and atmosphere during intervals of oceanic anoxia. Geology 33 (5), 397–400.
- Leavitt, W.D., Halevy, I., Bradley, A.S., Johnston, D.T., 2013. Influence of sulfate reduction rates on the Phanerozoic sulfur isotope record. Proc. Natl. Acad. Sci. USA 110 (28), 11244–11249.
- Lehrmann, D.J., Stepchinski, L., Altiner, D., Orchard, M.J., Montgomery, P., Enos, P., Ellwood, B.B., Bowring, S.A., Ramezani, J., Wang, H., Wei, J., Yu, M., Griffiths, J.D., Minzoni, M., Schaal, E.K., Li, X., Meyer, K.M., Payne, J.L., 2015. An integrated biostratigraphy (conodonts and foraminifers) and chronostratigraphy (paleomagnetic reversals, magnetic susceptibility, elemental chemistry, carbon isotopes and geochronology) for the Permian–Upper Triassic strata of Guandao section, Nanpanjiang Basin, South China. J. Asian Earth Sci. 108, 117–135.
- Luo, G., Kump, L.R., Wang, Y., Tong, J., Arthur, M.A., Yang, H., Huang, J., Yin, H., Xie, S., 2010. Isotopic evidence for an anomalously low oceanic sulfate concentration following end-Permian mass extinction. Earth Planet. Sci. Lett. 300 (1–2), 101–111.
- Lyons, T.W., Walter, L.M., Gellatly, A.M., Martini, A.M., Blake, R.E., 2004. Sites of Anomalous Organic Remineralization in the Carbonate Sediments of South Florida, USA: The Sulfur Cycle and Carbonate-Associated Sulfate. Vol. 379. Geological Society of America Special Papers, pp. 161–176.
- Marenco, P.J., 2007. Sulfur Isotope Geochemistry and the End Permian Mass Extinction. University of Southern California, pp. 199 Doctoral Dissertation.
- Marenco, P.J., Corsetti, F.A., Kaufman, A.J., Bottjer, D.J., 2008. Environmental and diagenetic variations in carbonate associated sulfate: an investigation of CAS in the lower Triassic of the western USA. Geochim. Cosmochim. Acta 72 (6), 1570–1582.
- Markovic, S., Paytan, A., Wortmann, U., 2015. Pleistocene Sediment Offloading and the global sulfur cycle. Biogeosciences 12 (10), 3043–3060.
- Mizutani, Y., Rafter, T.A., 1969. Oxygen isotopic composition of sulphates. Part 4, Bacterial fractionation of oxygen isotopes in the reduction of sulphate and in the oxidation of Sulphur: N. Z. J. Sci. 12, 60–68.
- Mizutani, Y., Rafter, T.A., 1973. Isotopic behaviour of sulphate oxygen in the bacterial reduction of sulphate. Geochem. J. 6 (4), 183–191.
- Monger, J., Wheeler, J., Tipper, H., Gabrielse, H., Harms, T., Struik, L., Campbell, R., Dodds, C., Gehrels, G., O'Brien, J., 1991. Upper Devonian to Middle Jurassic assemblages. In: Gabrielse, H., Yorath, C.J. (Eds.), Geology of the Cordilleran Orogen in Canada, Volume Geology of Canada, Part B. Cordilleran terranes. Geological Survey of Canada, pp. 281–327.
- Newton, R., Pevitt, E., Wignall, P., Bottrell, S., 2004. Large shifts in the isotopic composition of seawater sulphate across the Permo–Triassic boundary in northern Italy. Earth Planet. Sci. Lett. 218 (3–4), 331–345.
- Newton, R.J., Reeves, E.P., Kafousia, N., Wignall, P.B., Bottrell, S.H., Sha, J.-G., 2011. Low marine sulfate concentrations and the isolation of the European epicontinental sea during the early Jurassic. Geology 39 (1), 7–10.

- Nothdurft, L.D., Webb, G.E., Kamber, B.S., 2004. Rare earth element geochemistry of late Devonian reefal carbonates, Canning Basin, Western Australia: confirmation of a seawater REE proxy in ancient limestones. Geochim. Cosmochim. Acta 68 (2), 263–283
- Olivier, N., Brayard, A., Vennin, E., Escarguel, G., Fara, E., Bylund, K.G., Jenks, J.F., Caravaca, G., Stephen, D.A., 2016. Evolution of depositional settings in the Torrey area during the Smithian (early Triassic, Utah, USA) and their significance for the biotic recovery. Geol. J. 51 (4), 600–626.
- Orchard, M.J., 1984. Pennsylvanian, Permian, and Triassic conodonts from the Cache Creek Group, Cache Creek, Southern British Columbia. Curr. Res. 84, 197–206.
- Orchard, M.J., 2007. Conodont diversity and evolution through the latest Permian and early Triassic upheavals. Palaeogeogr. Palaeoclimatol. Palaeoecol. 252 (1–2), 93–117
- Orchard, M.J., Cordey, F., Rui, L., Bamber, E.W., Mamet, B., Struik, L.C., Sano, H., Taylor, H.J., 2001. Biostratigraphic and biogeographic constraints on the Carboniferous to Jurassic Cache Creek Terrane in Central British Columbia. Can. J. Earth Sci. 38 (4), 551–578
- Ovtcharova, M., Bucher, H., Schaltegger, U., Galfetti, T., Brayard, A., Guex, J., 2006. New Early to Middle Triassic U–Pb ages from South China: Calibration with ammonoid biochronozones and implications for the timing of the Triassic biotic recovery. Earth Planet. Sci. Lett. 243 (3–4), 463–475.
- Payne, J.L., Lehrmann, D.J., Wei, J., Orchard, M.J., Schrag, D.P., Knoll, A.H., 2004. Large perturbations of the carbon cycle during recovery from the end-Permian extinction. Science 305 (5683), 506–509.
- Present, T.M., Paris, G., Burke, A., Fischer, W.W., Adkins, J.F., 2015. Large Carbonate Associated Sulfate isotopic variability between brachiopods, micrite, and other sedimentary components in late Ordovician strata. Earth Planet. Sci. Lett. 432, 187–198.
- Rees, C.E., 1973. A steady-state model for Sulphur isotope fractionation in bacterial reduction processes. Geochim. Cosmochim. Acta 37 (5), 1141–1162.
- Rennie, V.C.F., Turchyn, A.V., 2014. The preservation of ³⁴S_{SO4} and ⁸O_{SO4} in carbonate-associated sulfate during marine diagenesis: A 25 Myr test case using marine sediments. Earth Planet. Sci. Lett. 395, 13–23.
- Riccardi, A.L., 2007. Carbonate-Associated Sulfate: Assessment of and Use as an Isotopic Proxy for Global Sulfur Cycling during End-Permian Mass Extinction. The Pennsylvania State University, pp. 146 Doctoral Dissertation.
- Romano, C., Goudemand, N., Vennemann, T.W., Ware, D., Schneebeli-Hermann, E., Hochuli, P.A., Bruhwiler, T., Brinkmann, W., Bucher, H., 2013. Climatic and biotic upheavals following the end-Permian mass extinction. Nat. Geosci. 6 (1), 57–60.
- Sano, H., Nakashima, K., 1997. Lowermost Triassic (Griesbachian) microbial bindstonecementstone facies. Southwest Japan. Facies 36 (1), 1–24.
- Sano, H., Onoue, T., Orchard, M.J., Martini, R., 2012. Early Triassic peritidal carbonate sedimentation on a Panthalassan seamount: the Jesmond succession, Cache Creek Terrane, British Columbia, Canada. Facies 58 (1), 113–130.
- Schobben, M., Joachimski, M.M., Korn, D., Leda, L., Korte, C., 2014. Palaeotethys seawater temperature rise and an intensified hydrological cycle following the end-permian mass extinction. Gondwana Res. 26 (2), 675–683.
- Schobben, M., Stebbins, A., Ghaderi, A., Strauss, H., Korn, D., Korte, C., 2015. Flourishing ocean drives the end-Permian marine mass extinction. Proc. Natl. Acad. Sci. USA 112 (33), 10298–10303.
- Schobben, M., Stebbins, A., Ghaderi, A., Strauss, H., Korn, D., Korte, C., 2016a. Eutrophication, microbial-sulfate reduction and mass extinctions. Commun. Integ. Biol. 9 (1), e1115162.
- Schobben, M., Ullmann, C.V., Leda, L., Korn, D., Struck, U., Reimold, W.U., Ghaderi, A., Algeo, T.J., Korte, C., 2016b. Discerning primary versus diagenetic signals in carbonate carbon and oxygen isotope records: an example from the Permian–Triassic boundary of Iran. Chem. Geol. 422, 94–107.
- Schobben, M., Stebbins, A., Algeo, T.J., Strauss, H., Leda, L., Haas, J., Struck, U., Korn, D., Korte, C., 2017. Volatile earliest Triassic sulfur cycle: a consequence of persistent low seawater sulfate concentrations and a high sulfur cycle turnover rate? Palaeogeogr. Palaeoclimatol. Palaeoecol. 486, 74-85.
- Schoepfer, S.D., Henderson, C.M., Garrison, G.H., Ward, P.D., 2012. Cessation of a productive coastal upwelling system in the Panthalassic Ocean at the Permian–Triassic Boundary. Palaeogeogr. Palaeoclimatol. Palaeoecol. 313–314, 181–188.
- Schoepfer, S.D., Henderson, C.M., Garrison, G.H., Foriel, J., Ward, P.D., Selby, D., Hower, J.C., Algeo, T.J., Shen, Y., 2013. Termination of a continent-margin upwelling system at the Permian–Triassic boundary (Opal Creek, Alberta, Canada). Glob. Planet. Chang. 105, 21–35.
- Sedlacek, A.R.C., Saltzman, M.R., Algeo, T.J., Horacek, M., Brandner, R., Foland, K., Denniston, R.F., 2014. ⁸⁷Sr, ⁸⁶Sr stratigraphy from the early Triassic of Zal, Iran: linking temperature to weathering rates and the tempo of ecosystem recovery. Geology 42 (9), 779–782.
- Shen J., Algeo T.J., Yuan S.L., Feng Q.L., Yu J.X., Zhou L., O'Connell B. and Planavsky N. J., In review Mercury enrichments provide evidence of Eearly Triassic volcanism following the end-Permian mass extinction, Earth Sci. Rev.
- Sim, M.S., Bosak, T., Ono, S., 2011. Large sulfur isotope fractionation does not require disproportionation. Science 333 (6038), 74–77.
- Snedden, J., Liu, C., 2010. A Compilation of Phanerozoic Sea-Level Change, Coastal Onlaps and Recommended Sequence Designations: Search and Discovery Article. pp. 40594.
- Song, H.J., Wignall, P.B., Tong, J.N., Bond, D.P.G., Song, H.Y., Lai, X.L., Zhang, K.X., Wang, H.M., Chen, Y.L., 2012. Geochemical evidence from bio-apatite for multiple oceanic anoxic events during Permian-Triassic transition and the link with end-Permian extinction and recovery. Earth Planet. Sci. Lett. 353, 12–21.
- Song, H.Y., Tong, J., Algeo, T.J., Horacek, M., Qiu, H., Song, H.J., Tian, L., Chen, Z.-Q., 2013. Large vertical $\delta^{13}C_{DIC}$ gradients in early Triassic seas of the South China craton:

ARTICLE IN PRESS

A. Stebbins et al. Earth-Science Reviews xxxx (xxxxx) xxxx—xxx

- Implications for oceanographic changes related to Siberian Traps volcanism. Glob. Planet. Chang. 105, 7–20.
- Song, H.Y., Tong, J., Algeo, T.J., Song, H.J., Qiu, H., Zhu, Y., Tian, L., Bates, S., Lyons, T.W., Luo, G., Kump, L.R., 2014. Early Triassic seawater sulfate drawdown. Geochim. Cosmochim. Acta 128. 95–113.
- Song, H.J., Wignall, P.B., Tong, J.N., Song, H.Y., Chen, J., Chu, D.L., Tian, L., Luo, M., Zong, K.Q., Chen, Y.L., Lai, X.L., Zhang, K.X., Wang, H.M., 2015. Integrated Sr isotope variations and global environmental changes through the late Permian to early late Triassic. Earth Planet. Sci. Lett. 424, 140–147.
- Stanley, S.M., 2009. Evidence from ammonoids and conodonts for multiple Early Triassic mass extinctions. Proc. Natl. Acad. Sci. USA 106 (36), 15264–15267.
- Stebbins, A., 2018. Understanding the Permian-Triassic Extinction and Recovery through the Sulfur Cycle: A Multiproxy Approach Using Pyrite and Carbonate-Associated-Sulfate. University of Massachusetts Boston Doctoral dissertation.
- Stebbins, A., Algeo, T.J., Krystyn, L., Brookfield, M., Williams, J., Nye, S., Hannigan, R., 2018. Marine Sulfur Cycle Evidence for Upwelling and Eutrophic Stresses during Early Triassic Cooling Events. (Submitted to Earth-Science Reviews, in review).
- Strauss, H., 1997. The isotopic composition of sedimentary sulfur through time. Palaeogeogr. Palaeoclimatol. Palaeoecol. 132 (1–4), 97–118.
- Struik, L.C., Schiarizza, P., Orchard, M.J., Cordey, F., Sano, H., MacIntyre, D.G., Lapierre, H., Tardy, M., 2001. Imbricate architecture of the upper Paleozoic to Jurassic oceanic Cache Creek Terrane, Central British Columbia. Can. J. Earth Sci. 38 (4), 495–514.
- Sullivan, L.A., Bush, R.T., McConchie, D.M., 2000. A modified chromium-reducible sulfur method for reduced inorganic sulfur: optimum reaction time for acid sulfate soil. Aust. J. Soil Res. 38 (3), 729–734.
- Sun, Y., Joachimski, M.M., Wignall, P.B., Yan, C., Chen, Y., Jiang, H., Wang, L., Lai, X., 2012. Lethally hot temperatures during the early Triassic greenhouse. Science 338 (6105), 366–370.
- Takahashi, S., Kaiho, K., Hori, R.S., Gorjan, P., Watanabe, T., Yamakita, S., Aita, Y., Takemura, A., Spörli, K.B., Kakegawa, T., Oba, M., 2013. Sulfur isotope profiles in the pelagic Panthalassic deep sea during the Permian–Triassic transition. Glob. Planet. Chang. 105, 68–78.
- Takahashi, S., Yamasaki, S.I., Ogawa, K., Kaiho, K., Tsuchiya, N., 2015. Redox conditions in the end-early Triassic Panthalassa. Palaeogeogr. Palaeoclimatol. Palaeoecol. 432, 15–28.
- Takano, B., 1985. Geochemical implications of sulfate in sedimentary carbonates. Chem. Geol. 49 (4), 393–403.
- Takemura, A., Sakai, M., Sakamoto, S., Aono, R., Takemura, S., Yamakita, S., 2007.
 Earliest Triassic radiolarians from the ARH and ARF sections on Arrow Rocks,
 Waipapa Terrane, Northland, New Zealand: the oceanic Permian/Triassic boundary
 sequence at Arrow Rocks (Ornatemanu). Northland. New Zealand. v. 24, 97–107.
- Tian, L., Tong, J.N., Algeo, T.J., Song, H.J., Song, H.Y., Chu, D.L., Shi, L., Bottjer, D.J., 2014. Reconstruction of early Triassic Ocean redox conditions based on framboidal

- pyrite from the Nanpanjiang Basin, South China. Palaeogeogr. Palaeoclimatol. Palaeoecol. 412. 68–79.
- Tong, J.N., Zuo, J.X., Chen, Z.Q., 2007. Early Triassic carbon isotope excursions from South China: proxies for devastation and restoration of marine ecosystems following the end-Permian mass extinction. Geol. J. 42 (3–4), 371–389.
- Wei, H., Shen, J., Schoepfer, S.D., Krystyn, L., Richoz, S., Algeo, T.J., 2015.
 Environmental controls on marine ecosystem recovery following mass extinctions, with an example from the early Triassic. Earth Sci. Rev. 149, 108–135.
- Wignall, P.B., Bond, D.P., Kuwahara, K., Kakuwa, Y., Newton, R.J., Poulton, S.W., 2010. An 80 million year oceanic redox history from Permian to Jurassic pelagic sediments of the Mino-Tamba terrane, SW Japan, and the origin of four mass extinctions. Glob. Planet. Chang. 71 (1–2), 109–123.
- Wignall, P.B., Bond, D.P.G., Sun, Y., Grasby, S.E., Beauchamp, B., Joachimski, M.M., Blomeier, D.P.G., 2015. Ultra-shallow-marine anoxia in an Early Triassic shallow-marine clastic ramp (Spitsbergen) and the suppression of benthic radiation. Geol. Mag. 153 (2), 316–331.
- Witts, J.D., Newton, R.J., Mills, B.J.W., Wignall, P.B., Bottrell, S.H., Hall, J.L.O., Francis, J.E., Crame, J.A., 2018. The impact of the Cretaceous-Paleogene (K-Pg) mass extinction event on the global sulfur cycle: evidence from Seymour Island. Antarctica 230, 17-45.
- Wotte, T., Shields-Zhou, G.A., Strauss, H., 2012. Carbonate-associated sulfate: experimental comparisons of common extraction methods and recommendations toward a standard analytical protocol. Chem. Geol. 326, 132–144.
- Yamakita, S., Takemura, A., Kamata, Y., Aita, Y., Hori, R., Campbell, H., 2007. A conodont biostratigraphic framework of a Permian/Triassic Ocean-floor sequence in the accretionary Waipapa terrane at Arrow Rocks, Northland, New Zealand: the Oceanic Permian/Triassic Boundary Sequence at Arrow Rocks (Oruatemanu) Northland, New Zealand. GNS Sci. Monogr. 24, 69–85.
- Zhang, L., Zhao, L., Chen, Z.Q., Algeo, T.J., Chen, J., Wang, R., Chen, L., Hou, J., Li, Y., Qiu, H., Feng, X., Lu, Z., Wang, X., Huang, Y., 2015. Amelioration of marine environments at the Smithian–Spathian boundary, Early Triassic. Biogeosci. Discuss. 12, 1597–1613.
- Zhang, G., Zhang, X., Hu, D., Li, D., Algeo, T.J., Farquhar, J., Henderson, C.M., Qin, L., Shen, M., Shen, D., Schoepfer, S.D., Chen, K., Shen, Y., 2017. Redox chemistry changes in the Panthalassic Ocean linked to the end-Permian mass extinction and delayed Early Triassic biotic recovery. Proc. Natl. Acad. Sci. USA 114 (8), 1806–1810.
- Zhang L., Orchard M.J., Algeo T.J., Chen Z.-Q., Lyu Z., Zhao L., Kaiho K., Ma B. and Liu SS., In press, An intercalibrated Triassic condont succession and carbonate carbon isotope profile, Kamura, Japan, Palaeogeogr. Palaeoclimatol. Palaeoecol.
- Zhang, L., Orchard, M. J., Brayard, A., Algeo, T. J., Zhao, L., Chen, Z.-Q., In review, The Smithian-Spathian boundary (late Early Triassic): a review and proposed definition: Earth Sci. Rev.